DOI: 10.1180/mgm.2025.10104

REVISION

'Basket-weave' textures formed during cooling of natural bornite: a HAADF STEM study

Samuel A. King[1,*], Cristiana L. Ciobanu[1], Nigel J. Cook[1], Ashley D. Slattery[2], Kathy Ehrig[1,3], Jie Yao[1], Yuri T. Campo Rodriguez[1,4]

[1]School of Chemical Engineering, The University of Adelaide, Adelaide, SA 5005, Australia

[2]Adelaide Microscopy, The University of Adelaide, Adelaide, SA 5005, Australia

[3]BHP Olympic Dam, 10 Franklin Street, Adelaide, SA 5000, Australia

[4]Geosciences Institute, University of Brasília DF, 70910-900, Brazil

Abstract

Bornite (Cu_5FeS_4) and digenite ($Cu_{9-x}Fe_xS_5$; x = 0.4) have closely related cubic structures and are known for their range of superstructures derived from metal vacancies leading to larger unit cells expressed as n × *a*, where *a* = ~5.5 Å and n is an integer. Such polymorphs can form during cooling from higher temperature bornite (Bn)–digenite (Dg) 1*a* solid solution (*ss*). The alleged basket-weave textures in natural bornite are investigated using high-angle annular dark field (HAADF) scanning transmission electron microscopy (STEM) imaging and energy-dispersive X-ray spectrometry. These techniques, combined with crystal modelling and STEM simulations, are suitable for depicting changes in phases related to

---

[*] Corresponding author. E-mail: samuel.king@adelaide.edu.au

crystal-structural modularity since they collectively better reproduce atomic distributions in real space. Bornite associated with either chalcocite or chalcopyrite from the Olympic Dam Cu-U-Au-Ag deposit, South Australia has non-stoichiometric Cu/Fe ratios and displays nanoscale basket-weave textures between the main components Bn2*a* and anilite (Cu_7S_4); Dg1*a* is preserved throughout, albeit as a minor phase. Anilite is a derivative of digenite, whereby $a = b = \sqrt{2}a_{Dg}$ and $c = 2a_{Dg}$. Two intermediate phases, Dg3*a* and Bn2*a*4*a*, are documented and an additional phase, Bn2*a*6*a*, is tentatively suggested to occur in Fe-rich nanodomains within Bn2*a*. Considering the epitaxial relationships between all phases, we infer that basket-weave textures record phase transitions via polymorphic transformations of parent Bn2*a* and Dg1*a* during cooling. Observed phase assemblages are thus linked to cooling of Bn-Dg$_{ss}$ in the range 70-87 mol.% Bn along a $Cu_{6.18}Fe_{1.26}S_5$ – $Cu_{9.12}Fe_{0.89}S_5$ tie-line defined from measured compositions. We depict three associations: Bn2*a* + Dg1*a*, Bn2*a*4*a* + Dg3*a*, and Bn2*a*4*a*/Bn2*a*6*a* + anilite, formed during cooling. Polymorph associations like these are relevant for enrichment of critical/precious metals in copper ores since Bi, Pb, Ag, Te, and, probably also Au, if dissolved in Bn-Dg$_{ss}$, could be incorporated into superstructures during Cu-Fe-sulphide phase transitions.

Keywords: basket-weave texture; bornite; digenite; anilite; superstructures; HAADF STEM

Introduction and Background

Bornite (Cu_5FeS_4) is a common component of copper ores and is often associated with digenite (Cu_9S_5), minerals of the chalcocite group ($Cu_{2-x}S$; x = 0 – 0.25) and chalcopyrite ($CuFeS_2$). Although digenite might be considered in the context of a solid solution with either bornite or chalcocite phases in the system Cu-Fe-S or Cu-S, the present work focuses on the bornite-digenite solid solution (Bn-Dg$_{ss}$). Natural digenite commonly contains small amounts of Fe (e.g., Morimoto and Koto, 1970). Bornite varies in abundance from being an accessory sulphide to the dominant ore mineral and displays textures ranging from lamellar to symplectitic (e.g., Ramdohr, 1969; Hatert, 2005; Cook *et al.*, 2011; Sharma *et al.*, 2020; Brodbeck *et al.*, 2022).

Prior studies emphasize that both bornite and digenite (see below) have polymorphs, and do not refer, specifically, to polytypes. Polytypism is considered a special case of polymorphism whereby two-dimensional translations within layers are preserved, while variation in lattice spacings normal to layers define distinct stacking sequences (e.g., Guiner *et al.*, 1984). Furthermore, the issue of polymorphism versus polysomatism (Hatert *et al.*, 2023) may also warrant further investigation in future studies of Cu-Fe-sulphides. Such topics are beyond the purpose of the present work.

Polymorphs of bornite (Bn) and digenite (Dg) are related to one another *via* crystal structural modularity with variable arrangements of cations within relatively stable sulphur frameworks. Most common are superstructures of both bornite and digenite derived by metal vacancies of various arrangement schemes leading to larger unit cells expressed as n × *a*, where $a = \sim 5.5$ Å and n is an integer (e.g., Pierce and Buseck, 1978). Although n ranges between 2 and 6, non-integer n values have also been speculated based upon electron diffraction (ED) patterns.

The nine common species currently defined by X-ray diffraction studies addressing crystal structures are: Bn1*a* (Tunell and Adams, 1949), Bn2*a* (Kanazawa *et al.*, 1978), Bn2*a*4*a* (Koto and Morimoto, 1975), Dg1*a* (Morimoto and Kullerud, 1963; Yamamoto and Kashida 1991; Will *et al.*, 2002), rhombohedral Dg5*a*-*R* (Cu_9S_5; Donnay *et al.*, 1958), anilite (Cu_7S_4; Koto and Morimoto, 1970), chalcocite, Cu_2S (both monoclinic and hexagonal; Evans, 1979; Will *et al.*, 2002), and djurleite ($Cu_{1.94}S$; Evans, 1979).

Bright field transmission electron microscopy (BF TEM) has been used to address the complexity of fine-scale intergrowths among Cu-(Fe)-sulphides. Particular emphasis has been placed on superstructuring that results from the ordering of metal vacancies and changes in the cation/sulphur ratios (e.g., Pierce and Buseck, 1978; Conde *et al.*, 1978; van Dyck *et al.*, 1980; Echigoya and Edington, 1982; Pósfai and Buseck, 1994; Ding *et al.*, 2005a, 2005b). *In-situ* electron beam experiments were used to investigate thermal behaviour controlling phase transformation among Cu-Fe-sulphides (Putnis and Grace, 1976; Putnis, 1977). Several other Bn2*a* superstructures have been constrained with the aid of *ab initio* models derived from Fe/Cu ordering schemes (Ding *et al.*, 2005a). The crystal structure of Bn4*a* was determined from TEM imaging and crystal structure simulations (Ding *et al.*, 2005b).

Morimoto and Kullerud (1966) assessed the system bornite-digenite at 350 °C. The phase diagram topology features a broad consolute solvus point defined at a mol. Bn:Dg ratio of 70:30 and ~ 340 ºC. The authors specified three intervals of phase associations from high temperature forms (325 – 205 ºC), to high-temperature Dg + low temperature Bn (205 – 120 ºC) and low temperature forms of digenite and bornite (< 120 ºC).

Following this pioneering work, several experimental studies, in combination with *in-situ* high-resolution neutron powder diffraction (HRPD) and differential scanning calorimetry (DSC), have addressed the behaviour of bornite-digenite series in terms of exsolution, phase transitions, controls of composition on the phase transition temperatures and redefinition of phase diagram (Grguric and Putnis, 1998, 1999; Grguric *et al.*, 1998, 2000). Six synthetic samples of different compositions along the bornite-digenite join were water quenched from above 600 ºC and interpreted from HRPD spectra to be mixtures of bornite and a low 5*a* digenite polymorph (Grguric and Putnis, 1999). Of relevance here is the optically visible basket-weave microtexture between bornite and digenite, obtained by annealing a sample of 90 mol.% bornite (Bn_{90}). This texture is explained as the result of coalescence of submicroscopic domains initially formed during quenching. The following intergrowths were identified by Grguric and Putnis (1999) in room temperature products: Bn2*a*4*a* in Bn_{100}, Bn2*a*4*a* and Dg1*a* in Bn_{90}–Bn_{30}, and Dg1*a* in Dg_{100}. The paucity of natural occurrences of intermediate compositions was thus interpreted as the result of "rapid kinetics of exsolution at geologically low temperatures".

In contrast to the quenched samples above, experiments using different annealing-cooling rates have shown the presence of four distinct assemblages for Bn_{90} based on HRPD: 1*a* solid solution (ss; unspecified phase) at 300 – 350 ºC; Bn2*a* + 1*a* ss at 190 – 225 ºC; Bn2*a*4*a* + 1*a* ss at 125 – 185 ºC, and Bn2*a*4*a* + Dg5*a* at 35 – 80 ºC (Grguric *et al.*, 2000). In their study, the authors used DSC scans of samples with 5 mol.% intervals along the bornite-digenite (Cu_5FeS_4–Cu_9S_5) join and within a 50 – 300 ºC temperature interval. Additionally, a HRPD study of the Bn_{90} assisted revision of the phase diagram for bornite-digenite solid solution. Based on this, the consolute point given by Morimoto and Kullerud (1966) was contested by Gruguric *et al.* (2000) and redefined at X = Cu_5FeS_4 and T = 265 ºC.

Symplectites between bornite and chalcocite are among the most intriguing ore textures. Although widespread in ores of different genetic types, they are typical of the giant iron-oxide copper gold (IOCG) deposit at Olympic Dam (Fig. 1A) and related systems of the Olympic Cu-Au Province, South Australia (e.g., Ciobanu *et al.*, 2011, 2017; Ehrig *et al.*, 2012; Owen *et al.*, 2018; King *et al.*, 2025a). Ciobanu *et al.* (2017) used the phase diagram of Morimoto and Kullerud (1966) to interpret symplectitic intergrowths between bornite and chalcocite in Olympic Dam ores. The study shows compositional differences between two distinct associations of bornite in the deposit, whereby excess (Cu+Fe)/S relative to stoichiometric Cu_5FeS_4 and deficit Cu/Fe ratios define bornite-chalcocite and bornite-chalcopyrite associations, respectively.

To identify discrete bornite and chalcocite polymorphs in Olympic Dam ore, Ciobanu *et al.* (2017) used BF TEM imaging on thinned foils prepared using dual focused ion beam (FIB) scanning electron microscopy (SEM). They concluded that the assemblages formed *via* exsolution from high temperature solid solutions in the system Cu-Fe-S, inferring that primary hypogene ore precipitation is preserved in the deposit, thus accounting for the observed vertical zonation pattern (Ehrig *et al.*, 2012; Fig. 1B). Zonation is preserved even though replacement relationships among Cu-(Fe)-sulphides are also widespread, as documented by electron backscatter diffraction study (King *et al.*, 2025b).

Intriguingly, a 'basket-weave network' was described from high-resolution TEM imaging of bornite that showed apparent micron-scale homogeneity (Ciobanu *et al.*, 2017). The authors questioned whether this was an artefact produced during FIB milling or rather a genuine intergrowth between bornite and djurleite (the presence of the latter being suggested by electron diffractions).

High angle annular dark field (HAADF) scanning TEM imaging is a relatively new technique capable of unlocking deep sub-ångstrom atomic resolution for phase characterisation when using contemporary aberration corrected improved instruments (Van Tendeloo *et al.*, 2012, and references therein). The HAADF STEM technique is especially well suited for structures comprising heavy atoms and has the advantage over BF TEM imaging in visualizing individual building modules from mineral series defined by crystal structural modularity, as shown for Pb-Bi sulphosalts (Ciobanu *et al.*, 2016). Although the basket-weave texture was also depicted by HAADF STEM imaging of bornite containing dense clausthalite (PbSe) inclusions (Owen *et al.*, 2018), the phase associations in such textures was not addressed.

This study employs HAADF STEM imaging and EDS analysis, combined with STEM simulations to better constrain the speciation and structures of phases forming the basket-weave textures in bornite, representative of the two associations in the Olympic Dam deposit. Refinement of phase relations in the system Cu-Fe-S and comparison between experiment and natural ores, as well as improved understanding of polymorph structures among Cu-(Fe)-sulphides, are valuable for at least two reasons. Firstly, a deeper appreciation of polymorph structures is relevant for understanding the mechanisms by which valuable minor metals are incorporated (King *et al.*, 2025a, 2025b). Secondly, this knowledge is a key prerequisite for attempts to use density functional theory (DFT) and molecular dynamics to shed light on the atomic-scale distributions of critical and precious metals within copper ores.

Samples and analytical methods

Nanoscale characterisation was undertaken on four polished sections containing bornite-chalcocite (RX6605 and CLC50a) and bornite-chalcopyrite (RX6610 and MV46) assemblages. These were prepared from samples of drillcore containing mineralization from across the Olympic Dam Breccia Complex, extending from the SE lobe of the deposit, through the 'barren' core to the NW lobe (Fig. 1A, B). These samples are representative of two of the three sulphide mineral zones at Olympic Dam: (i) shallower, bornite-chalcocite (Bn-Cc); and (ii) deeper, bornite-chalcopyrite (Bn-Ccp). The samples originate from three drillholes at different depths and are representative of the µm-scale intergrowths previously reported from Cu-Fe-ore at Olympic Dam (Fig. 1C-E).

Bornite-bearing assemblages were characterised at the micron-scale using reflected light microscopy and backscatter electron (BSE) imaging on a Hitachi SU1510 SEM to select suitable areas for nanoscale study. Scanning transmission electron microscope (STEM) sample preparation was performed using a FEI-Helios nanoLab Dual Focused Ion Beam and

SEM (FIB-SEM) to produce seven (< 100 nm) foils in procedures outlined by Ciobanu *et al.* (2011). A gallium source was used for slicing and thinning.

Each foil was analysed employing HAADF STEM imaging and energy-dispersive X-ray spectrometry (EDS)-STEM mapping using an ultrahigh-resolution, probe-corrected FEI Titan Themis S/TEM operated at 200 kV and equipped with a double-tilt holder. This instrument has a X-FEG Schottky source and Super- X EDS geometry. The Super-X EDS detector provides geometrically symmetric EDS detection with an effective solid angle of 0.8 sr. Probe correction delivered sub-ångstrom spatial resolution, and an inner collection angle > 50 mrad was used for HAADF imaging with a Fischione detector. A small spot size, either 7 or 9, was used for high-resolution imaging.

Velox software was utilised for image acquisition, including drift-corrected frame integration package (DCFI), and EDS data acquisition and processing. Various filters (Radial Wiener, Gaussian blur, High pass and Average) were used to eliminate noise. Quantification of the collected EDS spectra was performed using Thermo-Scientific Velox software (v3.15), which utilizes standard Cliff-Lorimer quantification and includes absorption correction optimized for both the Super-X detector geometry and the effect of sample holder shadowing for the double-tilt Super-X holder used. Quantification was performed using the Brown-Powell empirical ionization cross-section model and uncertainty values reported incorporate an estimated 20% error in the k-factors.

All instruments are housed at Adelaide Microscopy, The University of Adelaide.

Indexing of diffraction patterns was conducted with WinWulff (JCrystalSoft) and publicly available data from the American Mineralogist Crystal Structure Database (http://rruff.geo.arizona. edu/AMS/amcsd.php). Crystal structure models were generated in CrystalMaker. Annular dark field (ADF) image simulations were performed using STEM for the xHREM^{TM} (v5.3.2) software. Simulations for the empirical crystal models were obtained without thermal diffuse scattering (TDS) parameters (using Mott formula with Doyle-Turner X-Ray scattering factor). Electron diffraction simulations were generated using the multislice method and dynamical structure factor calculation.

Results and modelling

The Bn-Cc samples (RX6605 and CLC50a) consist of characteristic bornite with purple colour in reflected light that occurs with symplectites of chalcocite (Fig. 1C, D). The size and morphology of such symplectites vary widely within any given sample or location.

The Bn-Ccp samples (RX6610 – SE lobe and MV46 – NW lobe) consist of brown bornite (Fig. 1E, F), which comprises dense, sub-µm-scale lamellae of chalcopyrite. Although sample MV46 lacks such lamellae, it is considered part of the Bn-Ccp zone based on its position in the drillhole.

Relationships between Cu-Fe-sulphides and location of the FIB cuts from which STEM foils were prepared are illustrated in Figure 2. In both types of bornite, inclusions of Bi-(Pb)-tellurides, each only a few µm in width, are found either within bornite or at bornite-chalcocite boundaries. Four foils were obtained from Bn-Cc symplectites that range in size from fine (a few µm) to coarse (hundreds of µm) (Fig. 2A, B). Chalcocite from such symplectites either displays a homogenous grey-bluish colour or lamellar intergrowths with blue colouration (Fig. 2A, B). The two foils representing coarse Bn-Cc symplectites in the deeper sample (RX6605) were obtained across Bi-(Pb)-telluride Pb-Bi-chalcogenide lamellae enclosed within the symplectite (Fig. 2A). Two other foils representing the shallower Bn-Cc sample (CLC50a) were extracted from (i) the finest symplectites, and (ii) across the contact between bornite and lamellae of chalcocite (Fig. 2B).

Bornite from the deeper Bn-Ccp zone (RX6610), just ~ 21 m vertically below the Bn-Cc sample in the same drillhole (RD2852a), shows patches of colouration and lamellar intergrowths representative of both zone types (purple bornite with sub-µm-scale lamellar networks as well as brown bornite with chalcopyrite lamellae; Fig. 2C, D). In both cases, bornite displays domain heterogeneity with respect to size and density of included lamellae. The foil representing Bn-Ccp was extracted from across the contact between µm- to sub-µm-sized chalcopyrite lamellae within bornite (Fig. 2D).

The shallower sample from the Bn-Ccp zone (MV46) does not show µm-scale chalcopyrite inclusions but rather a Bi-(Pb)-telluride lamellae (Fig. 2E). The studied foil was obtained from across one of the coarser telluride grains (1 – 2 µm in width) (Fig. 2F). We note the presence of patchy areas with dark blue Cu-sulphides (Fig. 2E), which are distinct from the chalcocite forming the symplectites with bornite (Fig. 2A, B).

Nanoscale characterisation

The seven foils are shown in Figure S1 (Supplementary Material) and Table 1. A substructure made up of a fine two-phase mixture (each component some tens to a few hundreds of nm in size), recognizable by HAADF contrast as the aforementioned 'basket-weave' texture, is observed at the nanoscale throughout the bornite in all samples, including the foils from the Bn-Ccp zone. Only a few chalcopyrite lamellae are exposed within one of these foils (#6; Fig. S1). The basket-weave texture is rarely observed at the micron-scale (Fig. 2C). Curvilinear boundaries between bornite and chalcocite are observed in samples representing both the coarser and finer symplectites.

The basket-weave textures comprise two main components, bornite and anilite, with dark and bright contrast on HAADF STEM images, respectively. EDS STEM element maps of the basket-weave textures at various scales are shown in Figures 3 and 4. Compositions obtained from the maps for all species are listed in Table S1 and plotted in Figure S2.

We note that inclusions of Bi-(Pb)-chalcogenides are present in both the chalcocite and bornite or at their mutual contacts. The tellurides are tellurobismuthite (Bi_2Te_3) and aleksite ($Pb_2Bi_4Te_4S_4$), phases from the tetradymite (Cook *et al*., 2007a) and aleksite series (Cook *et al*., 2007b), respectively. Compositional data, imaging of layer stacking, and corresponding fast Fourier transform (FFT) patterns on $[11\bar{2}0]$ zone axis relevant for their identification (Ciobanu *et al*., 2009; Yao *et al*., 2023, 2024) are given in SM Table S1 and Figure S3.

At lower magnification, the densest basket-weave textures show intricate lamellar intergrowths between the two phases (Fig. 3A, B). We note a radial arrangement of the anilite at the edge of the tellurobismuthite lamella in this case (Fig. 3C).

In detail, the EDS STEM element maps show that the highest concentration of Cu corresponds to sets of short lamellae of anilite on the HAADF STEM image forming parallel arrays within a ‘mesh’ of intermediate Cu composition, i.e., between anilite (highest Cu content) and bornite (lowest Cu content) (Fig. 3D). Areas with intermediate Cu and Fe content are identified as digenite using high-resolution imaging (see below). More complex, network-like morphologies of the anilite arrays show comparable relationships with Cu and Fe distribution on EDS STEM maps (Fig. 3E). Interestingly, minor concentrations of Ag are noted within anilite lamellae that display a separation from bornite (Fig. 3F).

Figure 4 shows higher-resolution EDS STEM element maps of areas with still greater complexity. These comprise ultrathin, needle-like lamellae of a structurally distinct Cu-sulphide species, tentatively identified as the rhombohedral twin-structure of digenite 5*a* (Dg5*a*-*R*; Donnay *et al*., 1958) that crosscut the basket-weave anilite/digenite-bornite intergrowths (Fig. 4A) and chalcopyrite lamellae, when present (Fig. 4B). The EDS STEM maps show that the needles are compositionally indistinguishable from anilite in the basket-weave texture.

Secondly, the mapped distribution of Fe shows domains of enrichment relative to bornite. Such domains were found either adjacent to chalcopyrite (Fig. 4C) or anilite lamella (Fig. 4D). This lamellar substructure in anilite shows no compositional variation in terms of Cu concentration (Fig. 4D).

Compositional data obtained from the EDS STEM maps is listed in Table S1 and plotted on a series of Cu *vs.* Fe diagrams in Figure S2 (SM). Compositional data obtained from larger areas of bornite-anilite/digenite with basket-weave textures show either an excess or deficit of Cu relative to stoichiometric bornite, depending on whether the sample derives from the Bn-Cc or Bn-Ccp zones. This agrees with micron-scale EPMA data showing the same trends in bornite (Ciobanu *et al.*, 2017). Otherwise, bornite is relatively stoichiometric across all foils, except for the Fe-rich domains from the maps in Figure 4C, D. In the latter case, an average composition of ~ $Cu_4Fe_{1.8}S_{4.2}$ was obtained. Such stoichiometry is close to the $Cu_4Fe_2S_4$ formula considered for 2*a* bornite models by Ding *et al.* (2005a).

A compositional group, with average formula ~ $Cu_{9.12}Fe_{0.89}S_5$, was obtained from the areas of intermediate Cu content assessed as digenite from HR-STEM imaging (see below). Anilite has an average composition of ~ $Cu_{7.76}Fe_{0.22}S_{4.02}$. This is slightly richer in Cu than the compositional range attributed to anilite by Koto and Morimoto (1970), i.e., 7.00-7.36 Cu a.p.f.u. We also note the presence of minor Fe in anilite, which was absent in the data presented by Koto and Morimoto (1970). Nonetheless, there is a clear decrease in Fe, by roughly an order of magnitude, from digenite to anilite, and each of the species discussed above separate well on the Cu-Fe plots in Figure S2 (SM).

The average compositions of chalcopyrite and tellurobismuthite are close to stoichiometric (Table S1, SM).

Morphological variation among the basket-weave textures, comprising mainly bornite and anilite/digenite, is shown in Figure 5. The only exception texturally is the bornite with small blebs of digenite (Fig. 5A) that was obtained from the fine bornite-chalcocite symplectites in sample CLC50a (foil # 3; FIB cut 3 in Fig. 2B). The digenite blebs could not, however, be imaged at high resolution (because of foil thickness), and their identification as digenite is based solely on compositional data (Table S1, SM). The chalcocite species outside the bornite (Figs. 1A, B, S1A-D) is represented by the monoclinic Cu_2S polymorph and djurleite, thus structurally distinct from anilite and will be discussed elsewhere, based on a case study from a different ore deposit. Variation in morphology includes areas with parallel, dense sets of anilite lamellae in bornite (Fig. 5B, C). In most cases, digenite is present close to anilite-bornite contacts, and sometimes these phases are separated from one another by the Dg5*a*-*R* needles (Fig. 5D). The terminations of anilite arrays are often marked by small, lozenge shaped grains with well-defined composition (EDS STEM maps; inset Fig. 5D). Spectra for the bornite, digenite and anilite are shown in Figure 5E. The most complex basket-weave textures were observed in samples from the Bn-Ccp zone, in which the density of Dg5*a*-R needles is highest and can form parallel sets of two orientations (Fig. 5E). Unlike the example shown in Figure 5C, such needles can crosscut and displace both chalcopyrite and bornite + anilite/digenite textures (Fig. 5E). Notably, these needles do not crosscut the Fe-rich bornite even though they do crosscut all other phases (Fig. 5F).

High-resolution imaging

The images obtained in HAADF STEM mode show patterns in which the dots are directly attributable to individual atoms within the crystal structures. The signal intensity is proportional to the atomic number (Z) of an element, i.e., I ~ Z^2, and the number of atoms down the column on each respective site. Interpretation of images therefore requires well-constrained models of each analysed phase on relevant crystallographic orientations.

Bornite and digenite models

There exist several cubic crystal structure models for both bornite (Tunnel and Adams, 1949; Kanazawa *et al.,* 1978; Ding *et al.,* 2005a, 2005b) and digenite (Morimoto and Kullerud, 1963; Yamamoto and Kashida, 1991; Will *et al.,* 2002). Although these models share electron diffraction patterns, they can have different appearances on HAADF STEM images. The [110] zone axis is the optimal orientation for TEM identification of superstructuring in Cu-(Fe)-sulphides with cubic symmetry.

The bornite imaged throughout all foils corresponds to a 2-fold variety as depicted by satellite reflections on FFT patterns (Fig. 6A, B). In detail, the image displays a checkerboard arrangement of pairs of bright dots (Fig. 6C). The stoichiometric composition obtained for bornite studied here rules out the Bn2*a* models of Ding *et al.* (2005a) since these all consider a different stoichiometry (Cu_2FeS_2). The Bn2*a* model of Kanazawa *et al.* (1978) does not match either the observed HAADF STEM images (Fig. 6C), or simulations on the [110] zone axis (Fig. S4, SM). This model is built by 32 clusters of 7-atoms (4 Cu and 3 Fe) where each cluster has an overall occupancy of 1.5, placed internally into a S lattice. The orientation of atoms in the Cu-Fe clusters throughout the 2 × 2 × 2 supercell is however different to one another.

Using the same *Fm*3*m* space group as Kanazawa *et al.* (1978) but with atomic coordinates as in digenite (Yamamoto and Kashida, 1991), we created several 2*a* × 2*a* × 2*a* superstructure models in which the asymmetric unit cell comprises two groups of Cu+Fe atoms with different overall occupancy placed within interstices of the S lattice. We tested these models by STEM simulation.

The model that showed the best fit with analytical data is shown as a projection on [100] (Fig. 6D). This cube face shows two groups of atom clusters, either comprised of 4- or 3-atoms distributed around a central atom of higher occupancy. Using the crystallographic information file (cif) produced in CrystalMaker® we simulated both the electron diffraction and STEM image on the [110] zone axis (Fig. 6E).

The simulated image has a good match with the crystal structure model in terms of atomic weight of the clusters throughout the basic motif (Fig. 6E, F). The fit between the simulations (Fig. 6E) and data (Fig. 6G) is supported by the checkerboard arrangement of the two pairs of bright dots with ¼ *c* repeat, although, on the image, dots have a 'wavy' appearance. In detail, comparison between the simulation, model and image along the string of nine dots representing half the long diagonal of the rhombus motif re-emphasises this mismatch in terms of intensity/size of dots representing the two clusters and S atoms (Fig. 6H). Such discrepancies between the model/simulations and images could be addressed by further work involving density functional theory (DFT) calculation for the structure and TDS factors.

Imaging of areas with digenite composition on [110] zone axis (FFT with no satellite reflections) shows a different pattern than that of Bn2*a* (Fig. 7A). This image is recognisable from the atom-fill model (Fig. 7B) and displays an excellent match with the STEM simulation (Fig. 7C) using the structure of Yamamoto and Kashida (1991) with a composition of $Cu_{9.2}S_5$, even if natural digenite contains variable amounts of Fe (Pierce and Buseck, 1978). This structure, one of several published models, fits best with the STEM images. We also note the good match of the dot distribution along strings from the rhombus diagonal (image and STEM simulation) attributable to clustered Cu atoms and S columns (atom-fill model; Fig. 7D).

A digenite 3*a* superstructure was identified from FFT patterns and images on [110] zone axis (Fig. 7E). In this case, the three-fold satellite reflections correspond to rhombic-block partitioning on the image. Using the *Fm*3*m* digenite structure of Yamamoto and Kashida (1991), we built a three-fold superstructure in CrystalMaker®, incorporating Fe to match the obtained chemical data (Fig. 7F). The structure was assessed by simulations of electron diffraction and STEM images (Fig. 7G). The fit for the superstructure is reinforced by comparison between the image, simulation, and model along the string of 13 'dots' from the ½ length of the long diagonal of the rhombus motif (Fig. 7H). These dots represent the Cu, Cu/Fe atom clusters and S in the atom model.

Although the two new models (Bn2*a* and Dg3*a*) are empirical (cif files are provided in the SM) and require further assessment by other methods, e.g., *ab initio* calculations using DFT, they fit well with HAADF STEM observations.

Another bornite species identified in this study, is bornite 2*a*4*a*2*a* (in short Bn2*a*4*a*), also referred to as 'low-bornite' (Koto and Morimoto, 1975). Bn2*a*4*a* is isochemical with bornite but is the only bornite superstructure with orthorhombic symmetry (space group *Pbca*) (Koto and Morimoto, 1975). The observations could be modelled using the existing crystal structure.

The other phase of importance here is anilite (Cu_7S_4) which has been considered a low-temperature form of digenite with orthorhombic symmetry (Morimoto *et al.*, 1969; Koto and Morimoto, 1970). This is a superstructure of digenite, whereby $a = b = \sqrt{2}\, a_{Dg}$ and $c = 2a_{Dg}$, and shows a compositional range between Cu_7S_4 and $Cu_{7.36}S_4$ (Morimoto *et al.*, 1969). HAADF STEM images and FFTs are matched with simulations below.

Two-phase associations

Areas comprising approximately equal amounts of bornite and anilite/digenite with basket-weave texture, as well as those showing only an apparent single phase (bornite), were assessed by selected area electron diffraction (SAED) to evaluate their homogeneity over several hundred nm (Fig. 8). Irrespective of whether the image shows two- or single-phase domains (Fig. 8A, B), the SAED patterns show measurements corresponding to Bn2*a* on two major zone axes, [001] and [011], but with additional satellite reflections (Fig. 8C, E). In the case of $[001]_{\mathrm{Bn}2a}$ obtained from area shown in Figure 8A, the satellite reflections (Fig. 8C) can be attributed to intergrowths between bornite and anilite $[\bar{1}10]$ (see below). This is not the case for SAED patterns (Fig. 8D, E) obtained at different tilts from the apparently homogenous area of bornite in Figure 8B. On the SAEDs representing Bn2*a* on [011] and Bn2*a* on [112] zone axes, we can index the satellite reflections as bornite 2*a*4*a* on [101] and on [111] zone axis, respectively (Fig. 8D, E). The corresponding images show patterns illustrative of Bn2*a* (Fig. 8F) and Bn2*a*4*a* (Fig. 8G). To further understand how such images could be explained, we identified areas in which domains of the two bornite superstructures are separated from one another (Fig. 9).

Nanodomains of Bn2*a* and Bn2*a*4*a* were found as coherent intergrowths with one another on [101] and [111] zone axes. Although the images showing $[111]_{\mathrm{Bn}2a4a}$ and $[112]_{\mathrm{Bn}2a}$ are distinct for each phase (Fig. 9A), high-resolution images show curvilinear contacts with structural continuity along the planes $(\bar{1}\bar{1}1)$ and $(\bar{1}2\bar{1})$ in Bn2*a* and Bn2*a*4*a*, respectively. In detail, the two bornite species share motifs and FFT patterns (Fig. 9B, C) that could explain their appearance when overlapped as shown in Figure 8E, G.

When tilted, the same area also shows coherent intergrowths with curvilinear boundaries identified between $[110]_{\mathrm{Bn}2a}$ and $[101]_{\mathrm{Bn}2a4a}$, with structural continuity along $(1\bar{1}0)$ and $(\bar{1}01)$

planes, respectively (Fig. 9D). The two bornite superstructures show similar atomic arrangements, although with double periodicity along the ($\bar{1}01$) plane in Bn2*a*4*a*, but differ in the number of satellites on the FFT patterns (Fig. 9E, F). Such image similarities could explain their appearance when overlapped with one another (Fig. 8D, F). Figure 9G shows electron diffraction and STEM image simulations for the new zone axes in the two types of bornite.

Another type of two-phase association is represented by Bn2*a* and digenite (Fig. 10). Coherent contacts between these two phases (assessed by EDS spectra) were documented on two main zone axes, [100] and [110], both relevant for superstructure identification as depicted by FFT patterns and images (Fig. 10A, B). The correspondence between the main motifs is shown as overlays on cropped images obtained across these contacts. We note the good match between images on [110] zone axis for both phases with the models shown in Figures 6E and 7C. Some contacts between Bn2*a* and Dg1*a* are marked by nm-wide defects (Fig. 10C). In contrast to the above, on the [112] zone axis, the two phases display a marked difference on the images but are still coherently intergrown with one another (Fig. 10D).

Nanoscale domains of a Dg3*a* superstructure were found at the direct contact to Bn2*a* imaged on [110] zone axis (Fig. 11A). The FFT pattern over the area shows additional satellite reflections along 111* directions which are the result of combining three-fold digenite with two-fold bornite (Fig. 11A-C). The superstructure partitioning is shown on a crop obtained across the mutual contact (Fig. 11D). EDS spectra for each phase show the significant decrease in Fe from bornite to digenite (from 11.1 to 6.1 wt.% Fe; Fig. 11E).

Anilite with composition $Cu_{7.76}Fe_{0.22}S_{4.02}$ is the most prominent component forming coherent intergrowths with Bn2*a* in the basket-weave textures (Fig. 12). This phase occurs as lozenge-shaped domains within $[110]_{Bn2a}$ (Fig. 12A). Defects are also observed between the two phases (Fig. 12B). Fast Fourier transform patterns for such intergrowths show the match between 002*anilite ~ 002*Bn2*a* ~ 5.5 Å (Fig. 12C-E). However, the <hkl$_{\mathrm{Bn}2a}$> * with h, k, l=2n lattice vectors in Bn2*a* show extra satellites at ½ distances (Fig. 12C).

The FFT pattern in Figure 12E can be indexed as anilite on the $[\bar{1}20]$ zone axis (Fig. 12F). There is a relatively good fit between the STEM simulation of anilite and the HAADF STEM image (Fig. 12G, H). Additionally, there is a compositional difference of ~ 0.4 a.p.f.u. Cu and 0.22 a.p.f.u. Fe between the phase identified here as anilite relative to the ideal composition as defined by Koto and Morimoto (1970).

Likewise, the epitaxial relationships between the two main phases within the basket-weave textures were observed on a second orientation, $[100]_{\mathrm{Bn}2a}$ and $[\bar{1}10]_{\mathrm{An}}$ (Fig. 13 A-C). The FFT patterns show the match between the two phases whereby, <hk0$_{\mathrm{Bn}2a}$> * with *h*, *k*=2*n* lattice vectors in Bn2*a* show extra satellites at ½ distances (inset in Fig. 13A, Fig. 13B, C). The simulated electron diffraction and image show a good fit with the FFT pattern (Fig. 13B, D). The STEM simulations and image also show a relatively good match (Fig. 13E, F). $[\bar{1}10]_{\mathrm{An}}$ is also found in epitaxial contact with $[001]_{\mathrm{Ccp}}$ (Fig. 13G). Chalcopyrite from the same area (spectrum in Fig. 13H) shows domains of 2*a* superstructuring (Fig. 13I).

Bornite areas richer in Fe (Fig. 4C, D) show nanodomains with rhythmic banding of brighter and darker strips (Fig. 14). The first area (Fig. 14A) displays patterns resembling either Bn$_{na}$ or Dg$_{na}$ on [110] zone axes (Figs. 7, 8). The FFT pattern shows 6*a* and 2*a* modulations along 111* directions (Fig. 14B). Assuming such structures, the widths measured on the long diagonal at ~ 2 nm and 1 nm, respectively, could correspond to intergrowths between Dg4*a* and Bn2*a* superstructures (Fig. 14C). However, the Fe-rich composition of such domains, ~ $Cu_4Fe_2S_4$ (spectra in Fig. 14D), cannot be matched when considering Cu-rich digenite. It is likely the banded textures correspond to a superstructure of bornite, for example, 2*a*6*a*2*a*, and the observed HAADF contrast on the image is attributable to antiphase boundary relationships.

The second area also displays rhythmic strips of different HAADF contrast with a periodicity of ~ 6.2 Å and 12.3 Å for the dark and bright bands, respectively (Fig. 14E). The corresponding FFT pattern shows rectangular lattice vectors with 6- and 2-fold modulations relative to bright reflections at 3.1 Å and 1.9 Å (Fig. 14F). The distance 6 × 3.1 = 18.6 Å, is about the width of a bright + dark strip on the image (Fig. 14E). The image in Figure 14E is obtained close to the contact with Bn2*a* tilted on [112] zone axis (Fig. 14G). The two phases display epitaxy, whereby three lengths of <111> Bn2*a* are equal to one pair of bright and dark strips. The coherence between the two species is also illustrated by the FFT pattern (Fig. 14H) representing the intergrowths in Figure 14G.

Altogether, the two orientations show this bornite superstructure has 2-fold spacing on <001> and <110> lattice vectors and 6-fold on <111>, consistent with interpretation as a Bn2*a*6*a*2*a* superstructure. It could also be that such a superstructure is formed from pre-existing Bn2*a*4*a*, or by re-arrangement of Bn2*a*6*a*2*a*. Support for this interpretation can be seen in the image of Bn2*a*4*a* on [101] (Fig. 9E), which is comparable to the bright strips shown in Figure 14C.

Discussion

Why HAADF STEM?

There are around a dozen published TEM studies of Cu-(Fe)-sulphides using conventional BF imaging (e.g., Putnis and Grace, 1976; Putnis, 1977; Pierce and Buseck, 1978; Pósfai and Buseck, 1994; Ding *et al.*, 2005a, b; Ciobanu *et al.*, 2017; Owen *et al.*, 2018). While such studies are insightful for showing intergrowths between different species or the derivation of superstructures from a parent structure, the images are highly dependent upon thickness and focus. Moreover, the models produced for interpreting the images are not directly correlated with specific atomic positions (e.g., Pósfai and Buseck, 1997). In contrast, HAADF STEM imaging reproduces the atomic positions, which can be interpreted in tandem with crystal-structural models and simulations (e.g., Qin *et al*., 2024 and references therein).

The difference between HRTEM and HAADF STEM studies was also highlighted for pyrrhotites ($Fe_{1-x}S$, where $0.125 > x > 0.080$), in which vacancy ordering can induce crystal structural modifications. Pyrrhotites are a large group of sulphides in which slight changes in composition from stoichiometric FeS are accommodated by Fe vacancies and their ordering, resulting in different NC superstructures, with N (lattice parameter) being a multiple of NiAs-type subcell (e.g., Pósfai *et al*., 2000 and references therein). In the case of 4C pyrrhotite, ordering of Fe vacancies was resolved with atomic spatial resolution using HAADF STEM imaging (Xu *et al*., 2015). The direct imaging was further quantified/constrained by complementary STEM simulations (Jin *et al*., 2021). These results show that the earlier anti-phase boundary models derived from HRTEM studies (e.g., Harries *et al*., 2011) are more complex in nature.

In this study, we show that HAADF STEM imaging, especially if combined with EDS STEM analysis and element mapping, is an optimal choice for depicting crystal structures or superstructures in the bornite-digenite series. The cubic polymorphs of bornite and digenite are identifiable from their FFT or SAED patterns, but recognising the atomic arrangements within these structures is paramount for understanding phase associations among Cu-Fe-sulphides and the evolution of the assemblages they compose. We show how, despite several models being available, only some of them fit the STEM images, e.g., the choice for Dg1*a*. The results support the existence of the Bn2*a*4*a* superstructure originally proposed by Koto and Morimoto (1975), even though this had been subsequently dismissed by Ding *et al.* (2005b).

Ciobanu *et al.* (2017) recognised the nanoscale basket-weave texture in the same type of material from Olympic Dam, but their interpretation, based solely on SAEDs of djurleite in the basket-weave rather than anilite/digenite, as determined in the present study, was incorrect. Even if the identification of anilite requires more specific modelling, this species is clearly none of the monoclinic members or polymorphs of the chalcocite group.

Cooling history – the bornite-digenite system

The present study shows that 'bornite', with apparent homogeneity at the micron-scale, consists of two main components which are distinct from one another both compositionally and structurally. However, while the simplest bornite superstructure (2*a*) represents one of these, the second consists of a digenite species, if we consider anilite to be the low-T orthorhombic polymorph of digenite (Morimoto and Koto, 1970). Whereas cubic digenite is represented by two polymorphs, 1*a*- and 3*a* Dg, bornite has two orthorhombic polymorphs, 2*a*4*a*- and tentatively, 2*a*6*a* Bn, and only one cubic polymorph (2*a*). Epitaxial relationships between all these phases (Figs. 9-14) suggest they are formed by phase transition during cooling from Bn-Dg solid solution.

The plot in Figure S5 shows calculated basket-weave chemistry in terms of a Bn-Dg solid solution along a join between the mean measured compositions of the two endmembers as given in Table S1. The data cluster within the range ~ 87 and 70 mol.% Bn. The basket-weave compositions that show Fe in excess relative to the Bn-Dg tie-line are obtained from a domain containing chalcopyrite lamellae (Bn-Cp foil#6; map 9 on Fig. 4B) and from the Fe-rich bornite area in foil #7 (map 11 on Fig. 4D). Three of the six compositions representing Bn-Cc zone domains show an Fe deficit relative to the Bn-Dg tie-line. Such a result can be correlated with the abundance of anilite, which contains less Fe than the assumed digenite endmember.

The two published phase diagrams for the Bn-Dg solid solution (Morimoto and Kullerud, 1966; Grguric *et al*., 2000), although differing from one another in terms of topology and upper solvus temperature stability limit, both acknowledge three domains comprising polymorphs undergoing phase transition from high- to intermediate and low-temperature forms. Broadly, the two diagrams define the higher T interval by cubic Bn2*a* + Dg1*a*/1*a* ss, followed by cubic Dg (or 1*a* ss) + orthorhombic bornite (Bn2*a*4*a*), and high-order cubic Dg superstructures (5*a*Dg, 6*a*Dg) + Bn2*a*4*a* in the lowest T interval.

The new data show differences to the aforementioned diagrams, the most remarkable of which is the absence of any higher order cubic polymorphs of digenite. We show the persistent co-existence of two cubic polymorphs, 2*a*Bn and 1*a*Dg (Fig. 10), throughout all analysed material. Assuming this association is attributable to the earliest formed phases and considering the 87-70 mol% Bn composition interval for the basket-weave textures, we obtain upper temperature ranges of ~ 280 – 330 °C and 225 – 175 °C using the Bn-Dg diagrams of Morimoto and Kullerud (1966) and Gruguric *et al*. (2000), respectively. When bornite 2*a* undergoes phase transformation to a lower temperature polymorph, Bn2*a*4*a* co-existing with Bn2*a* (Fig. 9), high-temperature digenite 1*a* remains stable.

Formation of anilite as a low-temperature polymorph of digenite (Figs. 12, 13), below 120 °C or 80 °C, depending on which diagram we use, is part of the phase association in the low-T part of the diagram. At this stage, other low-temperature polymorphs could form. Indeed, we have imaged digenite 3*a* and the high-range superstructure of bornite tentatively considered as a 2*a*6*a*2*a* superstructure (Fig. 14).

The above interpretation, inferring that lower-T phases form as polymorphs of higher-T phases, is concordant with observed epitaxial relationships between all parent and derived structures.

Bornite 2*a* remains stable whereas Dg1*a* is present in minor amounts, having been extensively replaced by anilite. The excess Cu resulting from this transformation forms the basis for the occurrence of the latest chalcocite phase, tentatively identified as Dg5*a*-*R* (Donnay *et al*., 1958), that form as thin needles, often at boundaries between domains of bornite and anilite/digenite (Fig. 5B, C). Some of these needles however crosscut pre-existing assemblages (Figs. 4A, B, and 5F) and, in some cases, also offset their boundaries implying subsolidus movement or displacement during cooling.

Phase stability and transformations during cooling – the digenite debate

Initial separation between bornite and digenite within densely packed basket-weave textures could be the reason for preservation of Bn2*a* in greater proportions than Dg1*a*, which is largely replaced by anilite, assuming different kinetic rates of phase transformation. Natural digenite commonly contains small amounts of Fe and a metastable digenite-type solid solution of the 5.5*a* type can occur with digenite (Morimoto and Gyobu, 1971). The same authors carried out experiments on synthetic materials showing that the field of the homogeneous single phase with the *5a*-type structure (digenite *sensu stricto*) extends from 0.4 to 1.6 atom.% Fe and from 36.15 to 36.55 atom.% S at room temperature and this is centred on the composition $Cu_{6.9}Fe_{0.1}S_4$.

Whereas natural digenite containing Fe is only stable in the Cu-Fe-S system, digenite-type solid solution, this has a different stability field to digenite-type solid solution ($Cu_{1.75}S$–$Cu_{1.8}S$) in the system Cu-S, which is metastable relative to anilite at room temperature (Morimoto and Koto, 1970).

Two models of digenite transformation were proposed and debated in the literature from the 1960's and 1970's. The first model was based on X-Ray diffraction studies suggesting the role of twinning in digenite (transformation from cubic to rhombohedral symmetry; Donnay *et al.*, 1958) and the presence of Fe in controlling formation of either (i) intermediate superstructures (6*a*, 5*a*, 5.2*a*, 5.7*a*), or (ii) anilite (Morimoto *et al.*, 1969; Koto and Morimoto, 1970; Morimoto and Gyobu, 1971). The second model was based on TEM studies that dismissed the role of twinning (Putnis, 1977; Conde *et al.*, 1978). Conde *et al.* (1978) documented the existence of $2a_0$, $3a_0$, $4a_0$, $5a_0$, and $6a_0$, where a_0 is the (111) spacing in the cubic close-packed sulphur sublattice of synthetic digenite. These authors have also shown that periodic mixtures of 5*a* and 6*a* superstructures lead to non-rational spacings on SAEDs. Such state of disorder accounts for systematic extinctions in the diffraction patterns previously associated with twinning (Morimoto *et al.*, 1969; Morimoto and Koto, 1970). Putnis (1977) studied electron diffractions of natural digenite using heating-cooling experiments under the electron beam and demonstrated formation of a 6*a* digenite prior to any anilite superstructure, an irreversible transformation.

The data we present here shows there are substantial differences between the products of experimental studies and those occurring in natural assemblages, a key result that will be further discussed below. The presence of Bn2*a* in contact with all other species described here (Bn2*a*4*a*, Bn2*a*6*a*, Dg1*a*, Dg3*a*, and anilite; Figs. 9-14) implies that phase transformations are locally controlled over nanoscale domains. These transformations are, in turn determined by chemical (e.g., preferential distribution of trace elements such as the observed Ag in anilite/digenite; Fig 3F) and physical heterogeneity (e.g., radial arrangement of anilite beside telluride inclusions; Fig. 3C). We can also assume that the much slower cooling rates in natural systems relative to experiments would arrest some reactions e.g., the greater stability of the Bn2*a* parent relative to digenite 1*a*.

Higher-order bornite superstructures

A second type of nanoscale heterogeneity is represented by the occurrence of Fe-rich bornite displaying a conspicuous higher-order superstructure (2*a*6*a*2*a*). While questions remain about what triggers the different proportions between the two initially separated phases, bornite and digenite, it is feasible to assume they reflect distinct primary bulk Cu/Fe ratios and are thus readily applicable in most natural ores. If we assume the accuracy of this hypothesis, then the presence of Fe-rich bornite fields next to the highest density of anilite in the absence of Dg5*a*-*R* needles (Fig. 5B) could be interpreted as forming from the excess Fe produced during a transition from digenite to anilite.

Recrystallization of anilite as lamellar sets (Fig. 4D) is also tied to high-density phase separation. Such lamellae are atypical for the basket-weave texture, which is more typically characterised by lozenge-shaped, single grain morphology (Fig. 6A). The lamellar anilite may relate to late stages of bornite evolution, and indeed, the high-range Bn2*a*6*a* superstructure in the adjacent area (Fig. 14) may also indicate its formation as a low-T polymorph. A similar late formation of the Fe-rich bornite can be inferred from the second occurrence of such domains adjacent to chalcopyrite lamellae (Fig. 5G). In this case, the Fe-rich bornite area post-dates formation of Dg5*a*-*R* needles.

Summary and Implications

The key findings of this study are:

(1) The basket-weave texture in natural bornite with non-stoichiometric Cu/Fe ratios is real and not an artifact produced by sample preparation. Despite morphological and compositional variations, this texture comprises two main phases, Bn2*a* and anilite. Digenite 1*a* is preserved throughout, albeit as a minor phase.

(2) Two intermediate phases are documented as Dg3*a* and Bn2*a*4*a*. An additional phase, Bn2*a*6*a*, is tentatively suggested to occur in some Fe-rich nanodomains within Bn2*a*. The

latest phase, resembling the twin-digenite structure of Dg5*a* is not considered part of the basket-weave assemblage since it can crosscut phase boundaries of the main species.

(3) Empirical models for Bn2*a* and Dg3*a* are generated to match the HAADF STEM images and were assessed by STEM simulations. These will, however, require further assessment by *ab-initio* DFT crystal structure calculations.

(4) Epitaxial relationships between all phases indicate the basket-weave texture records phase transitions via polymorphic transformation of parent Bn2*a* and Dg1*a* during cooling. If we consider anilite as a structural derivative of Dg1*a*, the observed phase assemblages can be linked to cooling of bornite-digenite solid solutions with compositions in the range 87 – 70 mol.% along a $Cu_{6.18}Fe_{1.26}S_5$ – $Cu_{9.12}Fe_{0.89}S_5$ tieline defined from measured compositions.

(5) In the cooling scenario discussed in (4), there are three associations formed from high- to low temperature: Bn2*a* + Dg1*a*; Bn2*a*4*a* + Dg3*a*; and Bn2*a*4*a*/Bn2*a*6*a* + anilite. Preservation of inferred high-T phases implies slower cooling rates in natural environments than those reported in experimental studies, explaining the differences in specific polymorph associations.

(6) The crystallisation of Pb-Bi-(sulpho)tellurides prior to formation of basket-weave textures could have resulted from exsolution of various chalcophile elements and chalcogens dissolved in Bn-Dg solid solutions. Retention of lattice-bound Ag in Cu-rich phases suggests a correlation between crystal structures and minor element behaviour during cooling. We can speculate that Bn-Dg solid solutions would also scavenge Au from fluids, considering the high chalcophile affinity of this element.

Although well beyond the scope of the present study and requiring empirical confirmation, the aberrant behaviour of some Cu-(Fe)-sulphides in flotation circuits may plausibly be traced to subtle variations in structure and, by implication, to surface properties, in turn carrying major consequences for optimization of operational parameters.

The study shows the suitability and relevance of HAADF STEM techniques in assessing Cu-Fe-sulphide polymorphs as, for example, none of the existing Bn2*a* models in the literature could be matched by imaging and simulations. Minor and/or trace element incorporation within superstructures, a process promoted during phase transitions among Cu-Fe-sulphides, is a subject of high relevance for the enrichment of critical elements and precious metals in copper ores. We postulate that basket-weave textures and their nanoscale heterogeneity is the rule rather than exception in copper ores. The study also shows how digenite and its polymorphs form during hypogene ore processes rather than being tied to supergene alteration.

Acknowledgements. This research was funded by an Australian Research Council Linkage grant (LP200100156) to N.J.C. and K.E. The authors acknowledge Microscopy Australia for instrument access. Animesh Basak is thanked for technical support during FIB analysis. The authors appreciate the constructive comments from three anonymous reviewers and helpful insights from Associate Editor Owen Missen.

Supplementary materials: The following resources supporting this article can be found at https://doi.org/10.1180/mgm.XXXX.XX: Figures S1, S2, S3, S4, S5; Table S1; cif files for empirical models of bornite 2*a* and digenite 3*a*.

Competing interests. The authors declare none.

References

Brodbeck M., McClenaghan S.H., Kamber, B.S. and Redmond P.B. (2022) Metal(loid) Deportment in Sulfides from the High-Grade Core of the Bingham Canyon Porphyry Cu-Mo-Au Deposit, Utah. *Economic Geology*, **117**, 1521–1542.

Ciobanu C.L., Pring A., Cook N.J., Self, P., Jefferson D., Dima G.I. and Melnikov V. (2009) Chemical-structural modularity in the tetradymite group: A HRTEM study. *American Mineralogist*, **94**, 517–534.

Ciobanu C.L., Cook N.J., Utsunomiya S., Pring A. and Green L. (2011) Focussed ion beam–transmission electron microscopy applications in ore mineralogy: Bridging micro-and nanoscale observations. *Ore Geology Reviews*, **42**, 6–31.

Ciobanu C.L., Cook N.J., Maunders C., Wade B.P. and Ehrig K. (2016) Focused ion beam and advanced electron microscopy for minerals: Insights and outlook from bismuth sulphosalts. *Minerals*, **6**, 112.

Ciobanu C.L., Cook, N.J. and Ehrig K. (2017) Ore minerals down to the nanoscale: Cu-(Fe)-sulphides from the iron oxide copper gold deposit at Olympic Dam, South Australia. *Ore Geology Reviews*, **81**, 1218–1235.

Conde C., Manolikas C., Van Dyck D., Delavignette P., Van Landuyt J. and Amelinckx S. (1978) Electron microscopic study of digenite-related phases ($Cu_{2-x}S$). *Materials Research Bulletin*, **13**, 1055–1063.

Cook N.J., Ciobanu C.L., Wagner T. and Stanley C.J. (2007a) Minerals of the system Bi–Te–Se–S related to the tetradymite archetype: review of classification and compositional variation. *The Canadian Mineralogist*, **45**, 665–708.

Cook N.J., Ciobanu C.L., Stanley C.J., Paar W.H. and Sundblad, K. (2007b) Compositional data for Bi–Pb tellurosulfides. *The Canadian Mineralogist*, **45**, 417–435.

Cook N.J., Ciobanu C.L., Danyushevsky L.V. and Gilbert S. (2011) Minor elements in bornite and associated Cu-(Fe)-sulfides: a LA-ICPMS study. *Geochimica et Cosmochimica Acta*, **73**, 4761–4791.

Ding Y., Veblen D.R. and Prewitt C.T. (2005a) Possible Fe/Cu ordering schemes in the 2 a superstructure of bornite (Cu_5FeS_4). *American Mineralogist*, **90**, 1265–1269.

Ding Y., Veblen D.R. and Prewitt C.T. (2005b) High-resolution transmission electron microscopy (HRTEM) study of the 4a and 6a superstructure of bornite Cu_5FeS_4. *American Mineralogist*, **90**, 1256–1264.

Donnay G., Donnay J.D.H. and Kullerud, G. (1958) Crystal and twin structure of digenite, Cu_9S_5. *American Mineralogist*, **43**, 228–242.

Echigoya, J. and Edington, J.W. (1982) A transmission electron microscope study of the chalcocite-djurleite transformation in topotactically grown thin films of Cu_xS. *Physica Status Solidi*,**72**, 305–311.

Ehrig K., McPhie J. and Kamenetsky V.S. (2012) Geology and mineralogical zonation of the Olympic Dam iron oxide Cu–U–Au–Ag deposit, South Australia. In Geology and Genesis of Major Copper Deposits and Districts of the World, a Tribute to Richard Sillitoe. (Eds.) Hedenquist J.W., Harris M., Camus F., *Society of Economic Geologists: Littleton, CO, USA*, **16**, 237–268.

Evans H.T. (1979) The crystal structures of low chalcocite and djurleite. *Zeitschrift für Kristallographie*, **150**, 299–320.

Grguric B.A. and Putnis A. (1998) Compositional controls on phase-transition temperatures in bornite; a differential scanning calorimetry study. *The Canadian Mineralogist*, **36**, 215–227.

Grguric B.A. and Putnis A. (1999) Rapid exsolution behaviour in the bornite–digenite series, and implications for natural ore assemblages. *Mineralogical Magazine*, **63**, 1–12.

Grguric B.A., Putnis A. and Harrison R.J. (1998) An investigation of the phase transitions in bornite (Cu_5FeS_4) using neutron diffraction and differential scanning calorimetry. *American Mineralogist*, **83**, 1231–1239.

Grguric B.A., Harrison R.J. and Putnis, A. (2000) A revised phase diagram for the bornite-digenite join from in situ neutron diffraction and DSC experiments. *Mineralogical Magazine*, **64**, 213–231.

Guinier A., Bokij G.B., Boll-Dornberger K., Cowley J.M., Ďurovič S., Jagodzinski H., Krishna P., de Wolff P.M., Zyyagin B.B., Cox D.E., Goodman P., Hahn T., Kuchitsu K. and Abrahams S.C. (1984) Nomenclature of Polytype Structures. Report of the International Union of Crystallography Ad-Hoc Committee on the Nomenclature of Disordered, Modulated and Polytype Structures. *Acta Crystallographica*, **A40**, 399-404.

Harries D., Pollok K. and Langenhorst F. (2011) Translation interface modulation in NC-pyrrhotites: Direct imaging by TEM and a model toward understanding partially disordered structural states. *American Mineralogist*, **96**, 716–731.

Hatert F. (2005) Transformation sequences of copper sulphides at Vielsalm, Stavelot Massif, Belgium. *The Canadian Mineralogist*, **43**, 623–635

Hatert F., Mills S.J., Pasero M., Miyawaki R. and Bosi F. (2023) CNMNC guidelines for the nomenclature of polymorphs and polysomes. *Mineralogical Magazine*, **87**, 225-232.

Jin L., Koulialias D., Schnedler M., Gehring A.U., Pósfai M., Ebert P., Charilaou M., Schäublin R.E., Jia C.L., Löffler J.F. and Dunin-Borkowski R.E. (2021) Atomic-scale characterization of commensurate and incommensurate vacancy superstructures in natural pyrrhotites. *American Mineralogist*, **106**, 82–96.

Kanazawa Y., Koto K. and Morimoto N. (1978) Bornite (Cu_5FeS_4); stability and crystal structure of the intermediate form. *The Canadian Mineralogist*, **16**, 397–404.

King S.A., Cook N.J., Ciobanu C.L., Ehrig K., Gilbert S., Wade B. and Campo Rodriguez Y.T. (2025a) Trace element distributions among Cu-(Fe)-sulfides from the Olympic Dam Cu-U-Au-Ag deposit, South Australia. *Mineralium Deposita* https://doi.org/10.1007/s00126-024-01344-6

King S.A., Cook N.J., Ciobanu C.L., Ehrig K., Campo Rodriguez Y.T., Gilbert S. and Basak A. (2025b) EBSD mapping of Cu-Fe-sulfides reveal microstructures enriched in critical/precious metals and resolve deformation histories. *American Mineralogist* https://doi.org/10.2138/am-2024-9396

Koto K. and Morimoto N. (1970) The crystal structure of anilite. *Acta Crystallographica*, **B26**, 915–924.

Koto K. and Morimoto N. (1975) Superstructure investigation of bornite, Cu5FeS4, by the modified partial Patterson function. *Acta Crystallographica*, **B31**, 2268–2273.

Morimoto N. and Koto K. (1970) Phase relations of the Cu-S system at low temperatures: stability of anilite. *American Mineralogist*, **55**, 106–117.

Morimoto N. and Gyobu A. (1971) The composition and stability of digenite. *American Mineralogist*, **56**, 1889–1909.

Morimoto N. and Kullerud G. (1963) Polymorphism in digenite. *American Mineralogist*, **48**, 110–123.

Morimoto N. and Kullerud G. (1966) Polymorphism on the Cu_5FeS_4–Cu_9S_5 join. *Zeitschrift für Kristallographie*, **123**, 235–254.

Morimoto N., Koto K. and Shimazaki Y. (1969) Anilite, Cu_7S_4, a new mineral. *American Mineralogist*, **54**, 1256–1268.

Owen N.D., Ciobanu C.L., Cook N.J., Slattery A. and Basak A. (2018) Nanoscale study of clausthalite-bearing symplectites in Cu-Au-(U) ores: Implications for ore genesis. *Minerals*, **8**, 67.

Pierce L. and Buseck P.R. (1978) Superstructuring in the bornite-digenite series; a high-resolution electron microscopy study. *American Mineralogist*, **63**, 1–16.

Pósfai M. and Buseck P.R. (1994) Djurleite, digenite, and chalcocite: Intergrowths and transformations. *American Mineralogist*, **79**, 308–315.

Pósfai M. and Buseck P.R. (1997) Modular structures in sulphides: sphalerite/wurtzite-, pyrite/marcasite-, and pyrrhotite-type minerals. In Modular Aspects of Minerals. (Ed.) Merlino S., *EMU notes in Mineralogy*, **1**, 193–235.

Pósfai M., Sharp T.G. and Kontny A. (2000) Pyrrhotite varieties from the 9.1 km deep borehole of the KTB project. *American Mineralogist*, **85**, 1406–1415.

Putnis A. (1977) Electron diffraction study of phase transformations in copper sulfides. *American Mineralogist*, **62**, 107–114.

Putnis A. and Grace J. (1976) The transformation behaviour of bornite. *Contributions to Mineralogy and Petrology*, **55**, 311–315.

Qin L., Yang P., Jin Q., Yang C., Zhang J. and Yang Y. (2024) Real space method for HAADF image simulation. *Micron*, **185**, 103686.

Ramdohr P. (1969) The Ore Minerals and their Intergrowths. *Pergamon Press, Oxford* (1174pp.).

Sharma J.P., Sahoo P.R., Mahanta H., Venkatesh A.S. Babu E.V.S.S.K. and John M.M. (2020) Constraints on the genesis of the Proterozoic bornite dominated copper deposit from Nim ka Thana, western India: An IOCG perspective. *Ore Geology Reviews*, **118**, 103338.

Tunell G. and Adams C.E. (1949) On the symmetry and crystal structure of bornite. *American Mineralogist*, **34**, 824–829.

Van Dyck D., Conde-Amiano C. and Amelinckx S. (1980) The diffraction pattern of crystals presenting a digenite type of disorder. II. The structure of the digenite-related phases derived by means of the Cluster Theory. *Physica Status Solidi* **58**, 451–468.

Van Tendeloo G., Bals S., Van Aert S., Verbeeck J. and Van Dyck D. (2012) Advanced electron microscopy for advanced materials. *Advanced Materials* **24**, 5655–5675.

Will G., Hinze E. and Abdelrahman A.R.M. (2002) Crystal structure analysis and refinement of digenite, $Cu_{1.8}S$, in the temperature range 20 to 500 °C under controlled sulfur partial pressure. *European Journal of Mineralogy*, **14**, 591–598.

Xu H., Shen Z. and Konishi H. (2015) Natural occurrence of monoclinic Fe3S4 nano-precipitates in pyrrhotite from the Sudbury ore deposit: A Z-contrast imaging and density functional theory study. *Mineralogical Magazine*, **79**, 377–385.

Yamamoto K. and Kashida S. (1991) X-ray study of the average structures of Cu_2Se and $Cu_{1.8}S$ in the room temperature and the high temperature phases. *Journal of Solid State Chemistry*, **93**, 202–211.

Yao J., Ciobanu C.L., Cook N.J. and Ehrig K. (2023) Ab initio crystal structures and relative phase stabilities for the aleksite series, $Pb_nBi_4Te_4S_{n+2}$. *Acta Crystallographica*, **B79**, 482–494.

Yao J., Ciobanu C.L., Cook N.J., Ehrig K., Dima G.I. and Steinle-Neumann G. (2024) Ab initio calculations and crystal structure simulations for mixed layer compounds from the tetradymite series. *American Mineralogist*, **109**, 1375–1386.

Figure captions

Figure 1. (A) Map of the Olympic Dam deposit (location in the inset to the right) showing zoning of Cu-Fe-sulphides: pyrite-chalcopyrite (Py-Ccp), chalcopyrite-bornite (Ccp-Bn) and bornite chalcocite (Bn-Cc) within the Olympic Dam Breccia Complex (after Ehrig *et al.*, 2012). (B) Cross section (marked by line in A), showing the vertical sulphide zonation in the deepest part of the deposit. (C-F) Reflected light images of the four samples showing aspects of the Cu-(Fe)-sulphides within hematite

(Hem) breccias from ore zones as labelled. Note bornite forming symplectites of variable size/morphology with chalcocite in C and D. Apparently homogenous bornite is typical of grains from the Bn-Ccp zone (E, F).

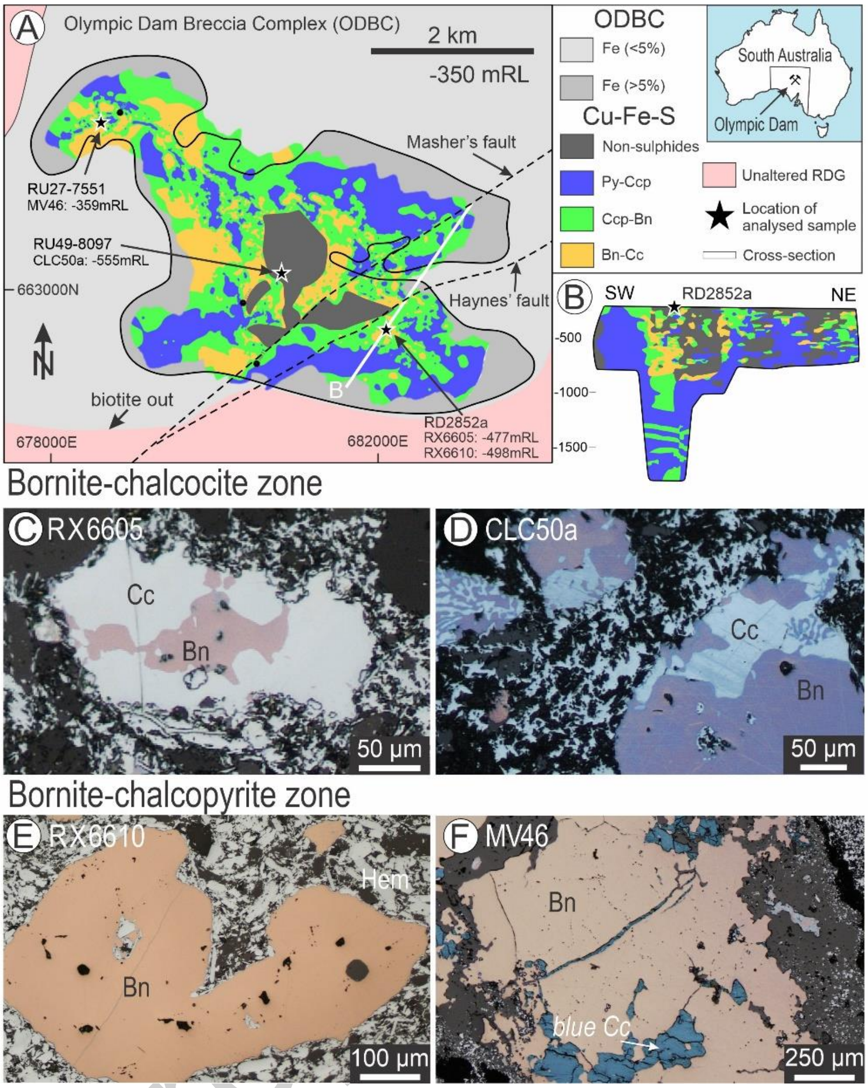

Figure 2. Reflected light (A-E) and BSE (F) images showing petrographic aspects of areas sampled for nanoscale study. White rectangles represent location of FIB cuts from which slices were lifted and prepared as thin foils. (A, B) FIB cuts placed across Bn-Cc boundaries and within bornite alone (cut 2) targeted fine and coarse symplectites as well as telluride inclusions positioned at mutual contacts. (C-F) FIB cuts in apparently homogenous bornite targeted fine lamellar networks in C and D or telluride inclusions in E. Detail of tellurides in F. The lamellar networks were identified as chalcopyrite (Ccp) only in the coarser lamellae domain from D (cut 6), even though all these grains

were collected from Bn-Ccp ore zone. This shows the patchy distribution of the sulphide associations at the micron-scale throughout the orezones defined based on assays. Fractures and secondary Cu-sulphides (blue chalcocite?) are present in bornite from C and E. Abbreviations: Pb-Bi-chalc. – Bi-sulphotelluride from the aleksite series; Tbi–tellurobismuthite.

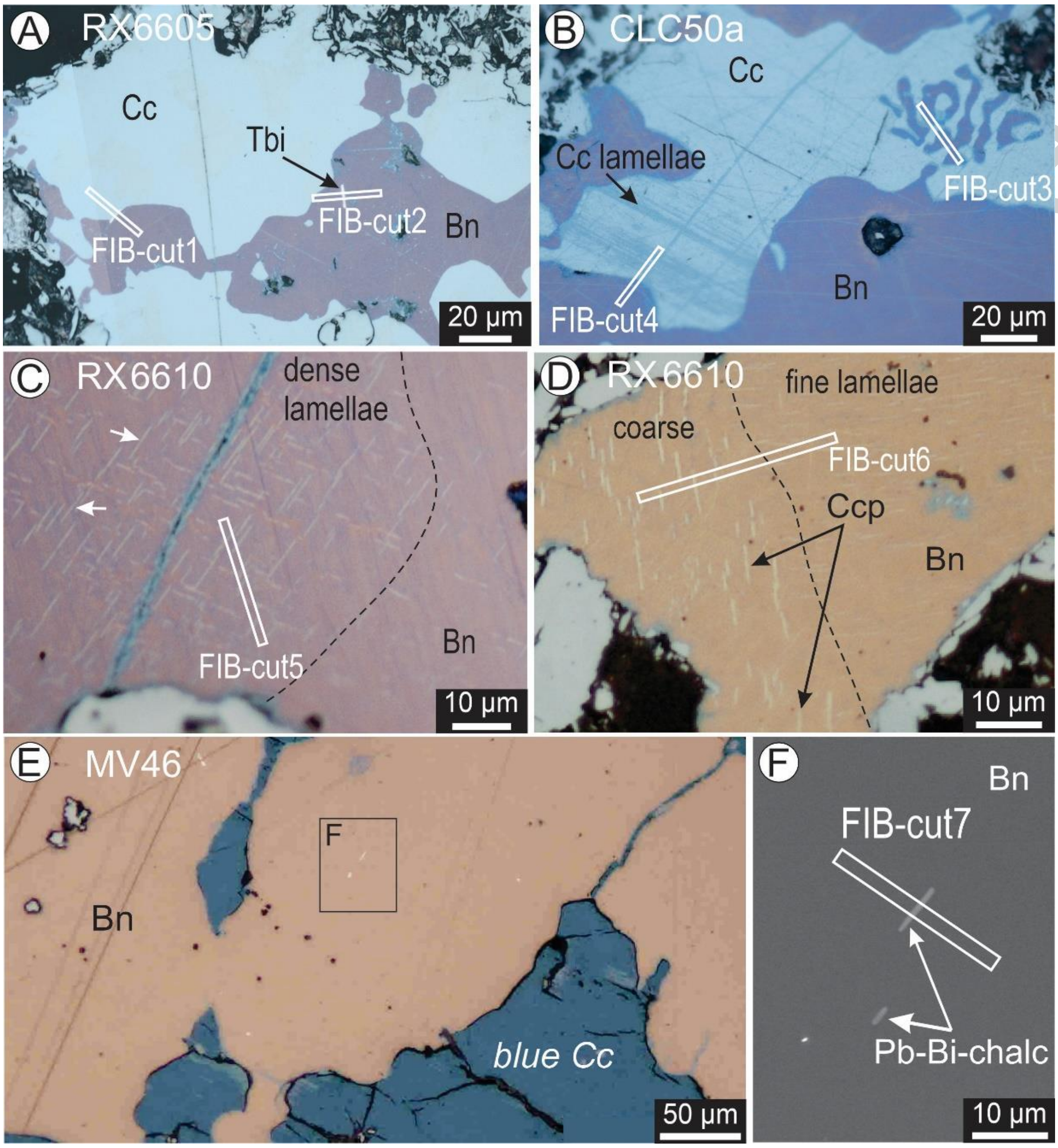

Figure 3. HAADF STEM images and corresponding EDS STEM maps of basket-weave textures. Numbers correspond to maps labelled in Figure S1. (A, B) Dense networks of Cu-rich lamellae (anilite (An) + digenite (Dg) in bornite (Bn; Fe-rich host phase). (C) Tellurobismuthite (Tbi) inclusions surrounded by a radial network of Cu-rich lamellae. (D-F) Details of basket-weave textures showing variable Cu-compositions attributable to presence of both anilite and digenite. Note short

lamellar arrays of anilite in (D). Profile across a single lamella of anilite/digenite shows enrichment in Ag in (F).

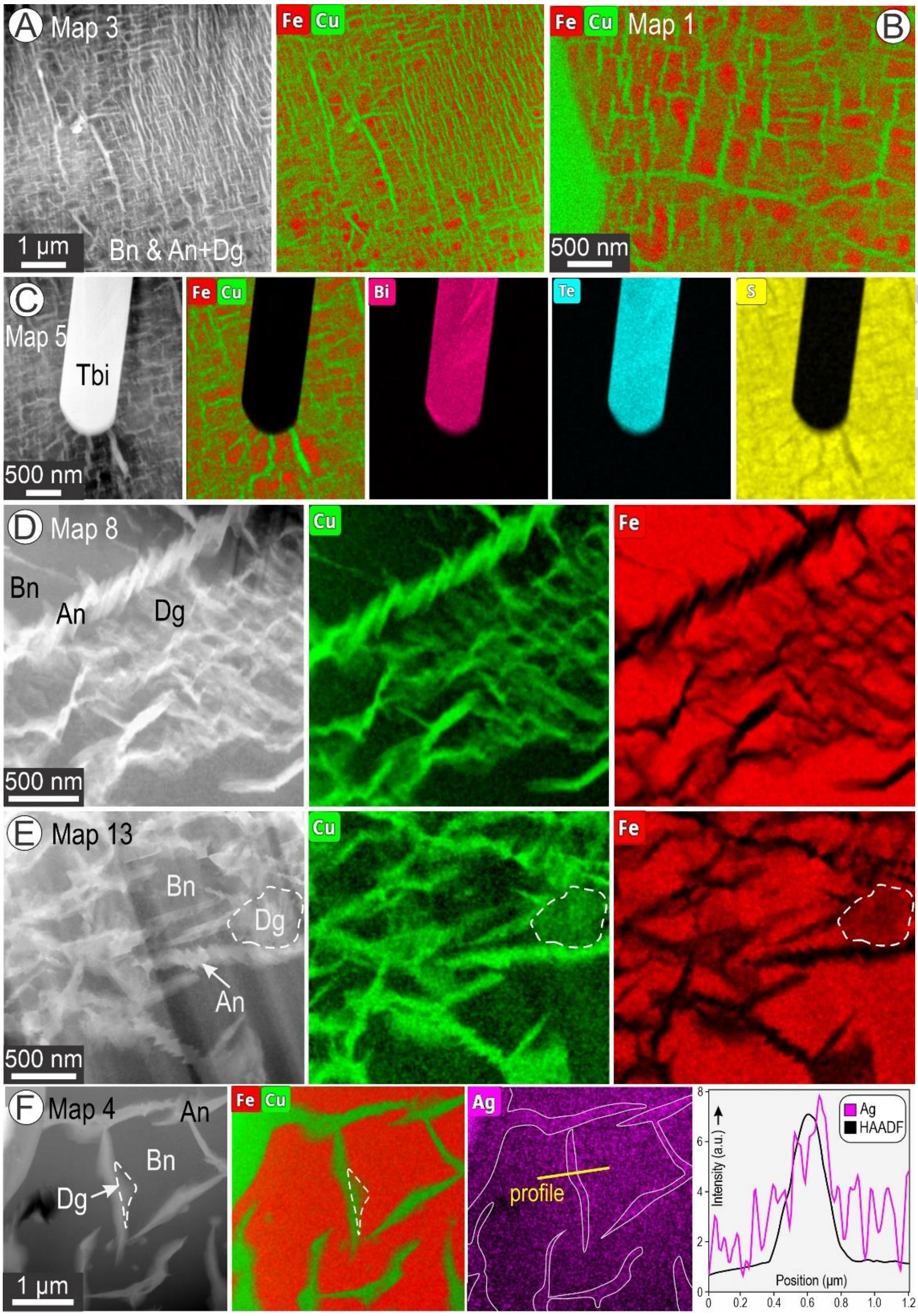

Figure 4. Higher resolution EDS STEM maps showing further details of basket-weave textures. (A, B) Copper-bearing needles (arrowed) crosscutting bornite (Bn) and anilite (An) + digenite (Dg) boundaries as well as a chalcopyrite lamella (Ccp) in (B). The needles are attributed to the

rhombohedral twin-structure of digenite 5*a* (Dg5*a*-*R*) of Donnay *et al.* (1958). (C-D) Fe-rich domains in bornite next to a chalcopyrite lamella in (C) and a set of anilite lamellae of different orientations in (D).

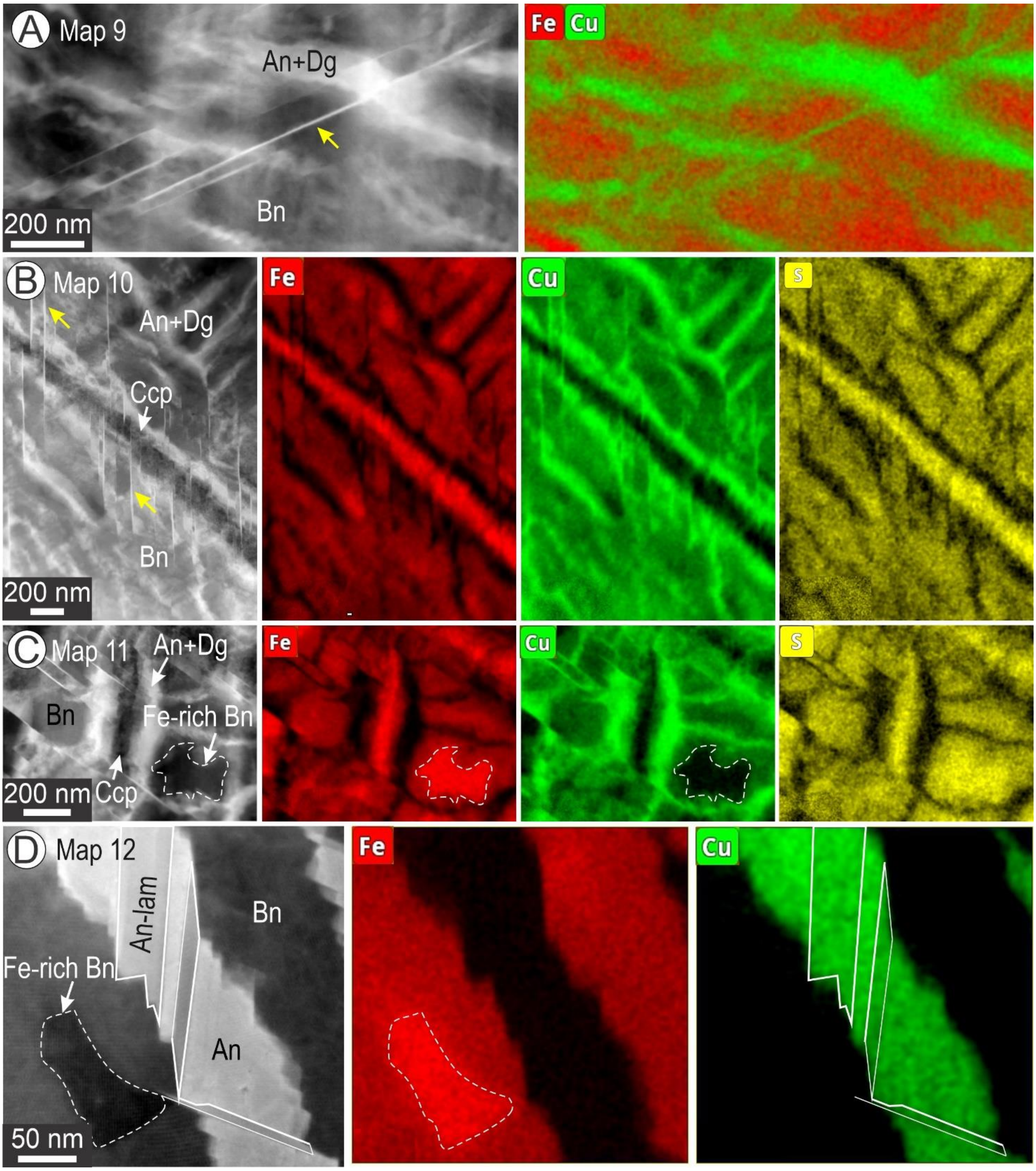

Figure 5. Low-magnification images (HAADF STEM and BF in C), except map + spectra in (E) showing textural variation between main components in the basket-weave textures. (A) Blebby

inclusions of digenite (Dg) in bornite (Bn) forming finer symplectites with chalcocite from sample CLC50a (FIB cut 3/foil 3 in Figs. 2B and S1). (B, C) Parallel sets of anilite (+digenite) lamellae adjacent to the Fe-rich bornite domains. Note the different orientations of such lamellae well depicted on the BF STEM image in (C). (Typical lozenge-shaped anilite (An) within bornite and digenite. Note the very low HAADF contrast between bornite and digenite separated by a needle of Dg5*a*-*R* (arrowed). (E) Fe-Cu overlay map of anilite from (D) and spectra (Sp.) of the three phases as labelled. Note the decreasing Fe content from bornite to digenite and anilite. (F) Network of Dg5*a*-*R* needles (arrowed) crosscutting the phases forming the basket-weave texture and an embedded chalcopyrite lamella (Ccp). (G) Lobate-shaped Fe-rich domain in bornite close to a chalcopyrite lamella. Note the adjacent Dg5*a*-*R* needle (arrowed) does not cut this domain.

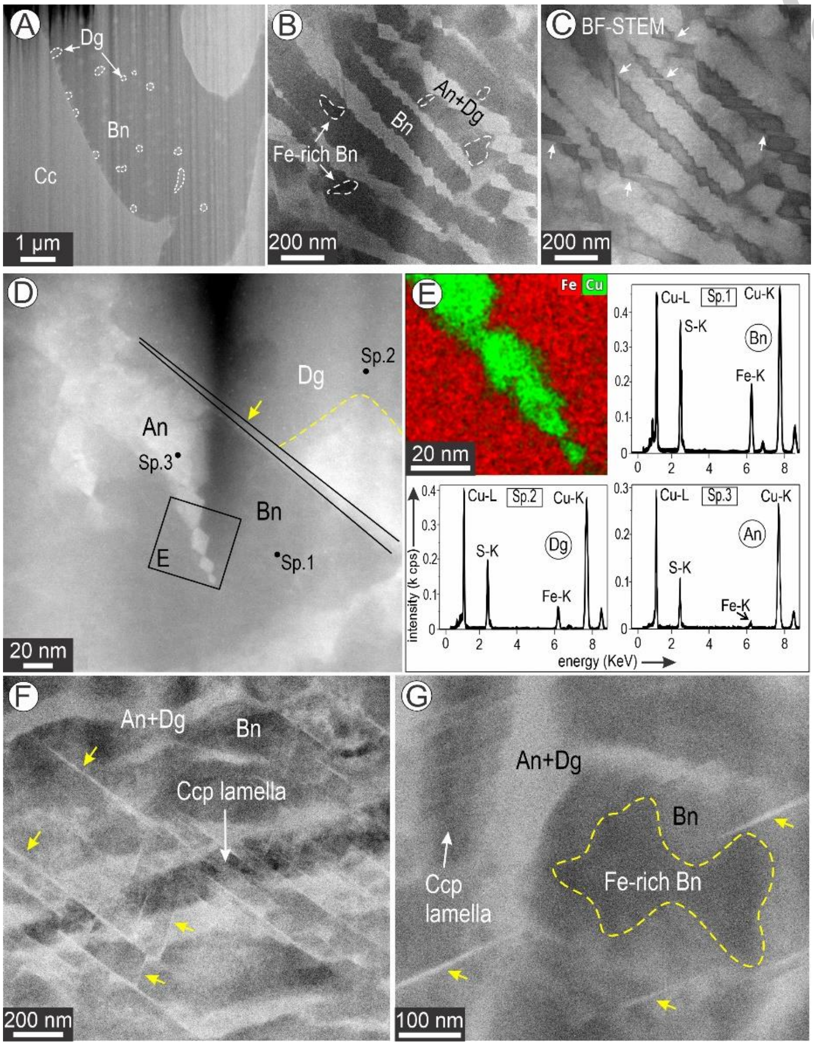

Figure 6. Analytical data (A-C), models and simulation for bornite 2*a* (Bn2*a*) superstructure (D-H). (A) High-resolution HAADF STEM image of Bn2*a* host to a lozenge-shaped anilite (An). (B) Fast Fourier transform (FFT) pattern obtained from area marked by rectangle in (A) showing the 2-fold satellite reflections (circled) along 111* directions on $[110]_{\text{bornite}}$. (C) Crop from (A) showing the rhombus motif (yellow) defining the Bn2*a* superstructure. (D) Atom filled model showing the cluster arrangements for metals (M) of occupancies as labelled. (E, F) Electron diffraction (ED) and STEM simulation (E) and atom fill structure (F) for the empirical Bn2*a* model. (G) FFT pattern and image matching the proposed model. (H) Comparison of simulation, model and image showing atom distributions along the half-cell outlined by the rectangles in (E-G). Dashed line shows the rhombus motif for the superstructure on [110] zone axis. Note that the simulation shows decreasing brightness/size of dots for C1, S and C2 (very faint) in agreement with their calculated intensity as 650, 256 and 202 arbitrary units, respectively. In contrast, the image shows intensity/size of C2 and S approximately equal, but 2 of the 4 sulphur atoms are not displayed.

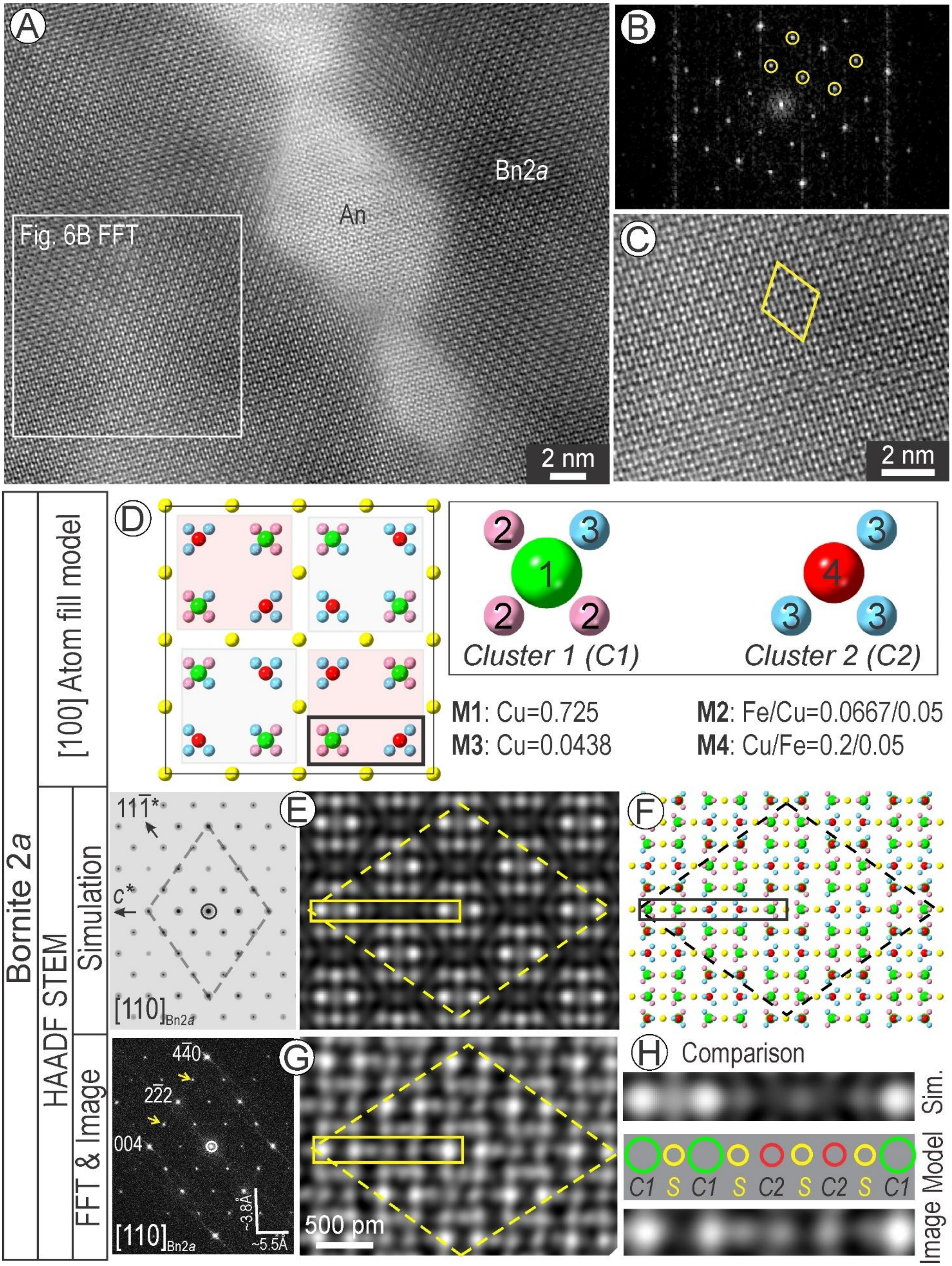
A
Fig. 6B FFT
An
Bn2a
2 nm
B
C
2 nm
Bornite 2a
[100] Atom fill model
HAADF STEM
Simulation
FFT & Image
D
2
3
1
2
2
Cluster 1 (C1)
3
4
3
3
Cluster 2 (C2)
M1: Cu=0.725
M2: Fe/Cu=0.0667/0.05
M3: Cu=0.0438
M4: Cu/Fe=0.2/0.05
$11\bar{1}^*$
c^*
$[110]_{Bn2a}$
E
F
G
$4\bar{4}0$
$2\bar{2}2$
004
~3.8Å
~5.5Å
$[110]_{Bn2a}$
500 pm
H Comparison
Sim.
Model
Image
C1 S C1 S C2 S C2 S C1

Figure 7. Analytical data, models and simulations for digenite 1*a* (Dg1*a*) (A-D) and Dg3*a* superstructure (E-H). FFT pattern, image (A) and atom fill model (B) using the Yamamoto and Kashida (1991) structure for Dg1*a*. (C) ED and STEM simulations for Dg1*a*. (D) Comparison of image, simulation and model showing atom distributions along the direction outlined by the rectangles in (A-C). (E, F) FFT pattern, image (E) and atom fill model for empirical Dg3*a* in (F). (G) ED and STEM simulations for Dg3*a*. (H) Comparison of image, simulation and model showing atom distributions along the half-cell outlined by the rectangles in (E-G). Dashed line shows the rhombus motif for the (super)structure on [110] zone axis.

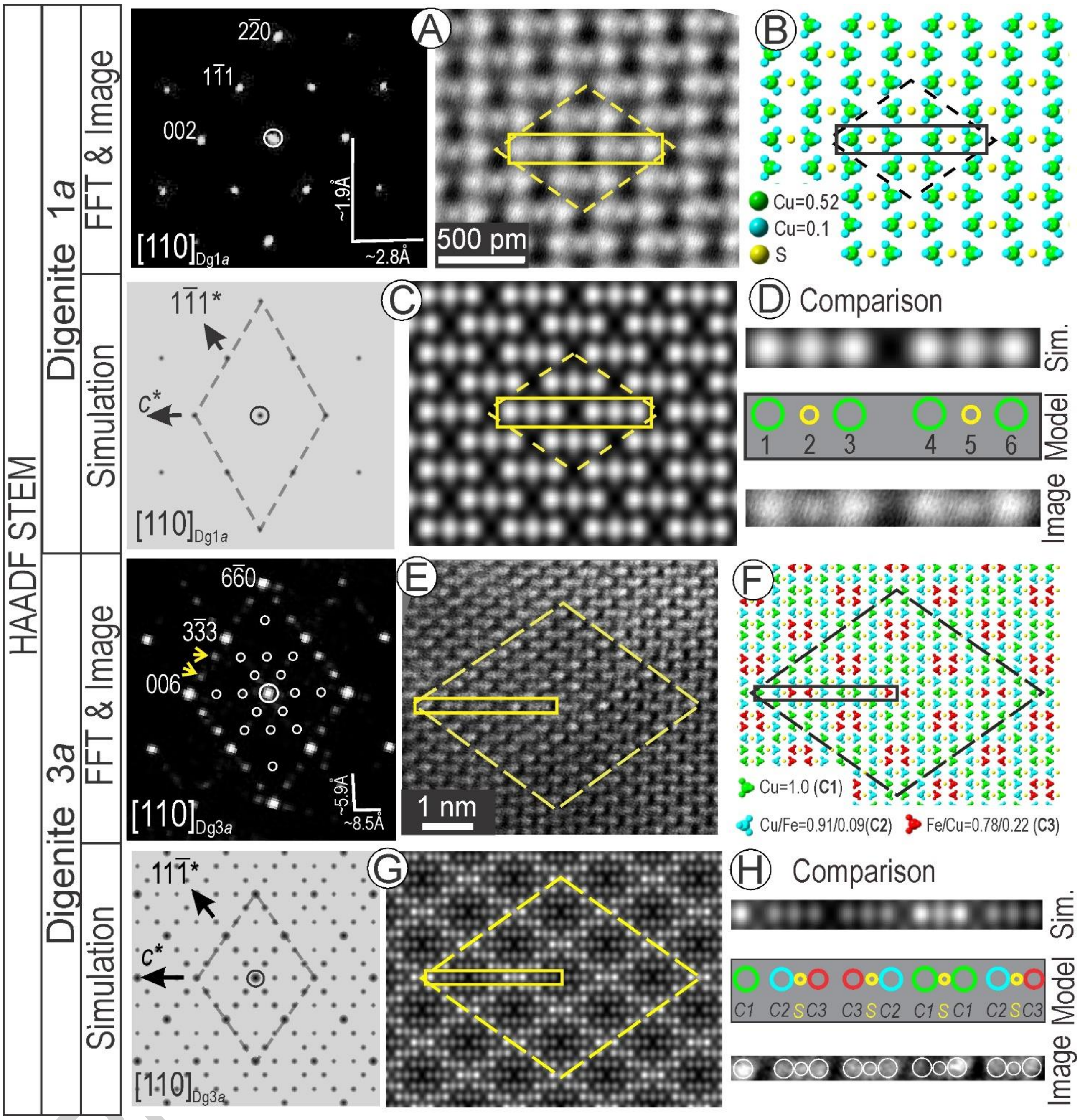
HAADF STEM
Digenite 1a
FFT & Image
Simulation
Digenite 3a
FFT & Image
Simulation
A
2$\bar{2}$0
1$\bar{1}$1
002
~1.9Å
~2.8Å
[110]$_{Dg1a}$
500 pm
B
Cu=0.52
Cu=0.1
S
C
1$\bar{1}$1*
c*
[110]$_{Dg1a}$
D Comparison
Sim.
Model
1 2 3 4 5 6
Image
E
6$\bar{6}$0
3$\bar{3}$3
006
~5.9Å
~8.5Å
[110]$_{Dg3a}$
1 nm
F
Cu=1.0 (C1)
Cu/Fe=0.91/0.09(C2)
Fe/Cu=0.78/0.22 (C3)
G
11$\bar{1}$*
c*
[1$\bar{1}$0]$_{Dg3a}$
H Comparison
Sim.
Model
C1 C2 S C3 C3 S C2 C1 S C1 C2 S C3
Image

Figure 8. Low-magnification images (A, B), selected area electron diffractions (SAED) patterns (C-E) and high-resolution HAADF STEM images of bornite (Bn) (F, G) representing two-phase basket-weave textures. Circles on (A) and (B) show the area from which the SAEDs were obtained. (C-E) SAEDs showing intergrowths between two phases on zone axes as labelled. (F, G) Images corresponding to SAEDs representing the Bn2*a*+Bn2*a*4*a* obtained from (B) show a single phase as labelled (either Bn2*a* or Bn2*a*4*a*) depending on the specimen tilt.

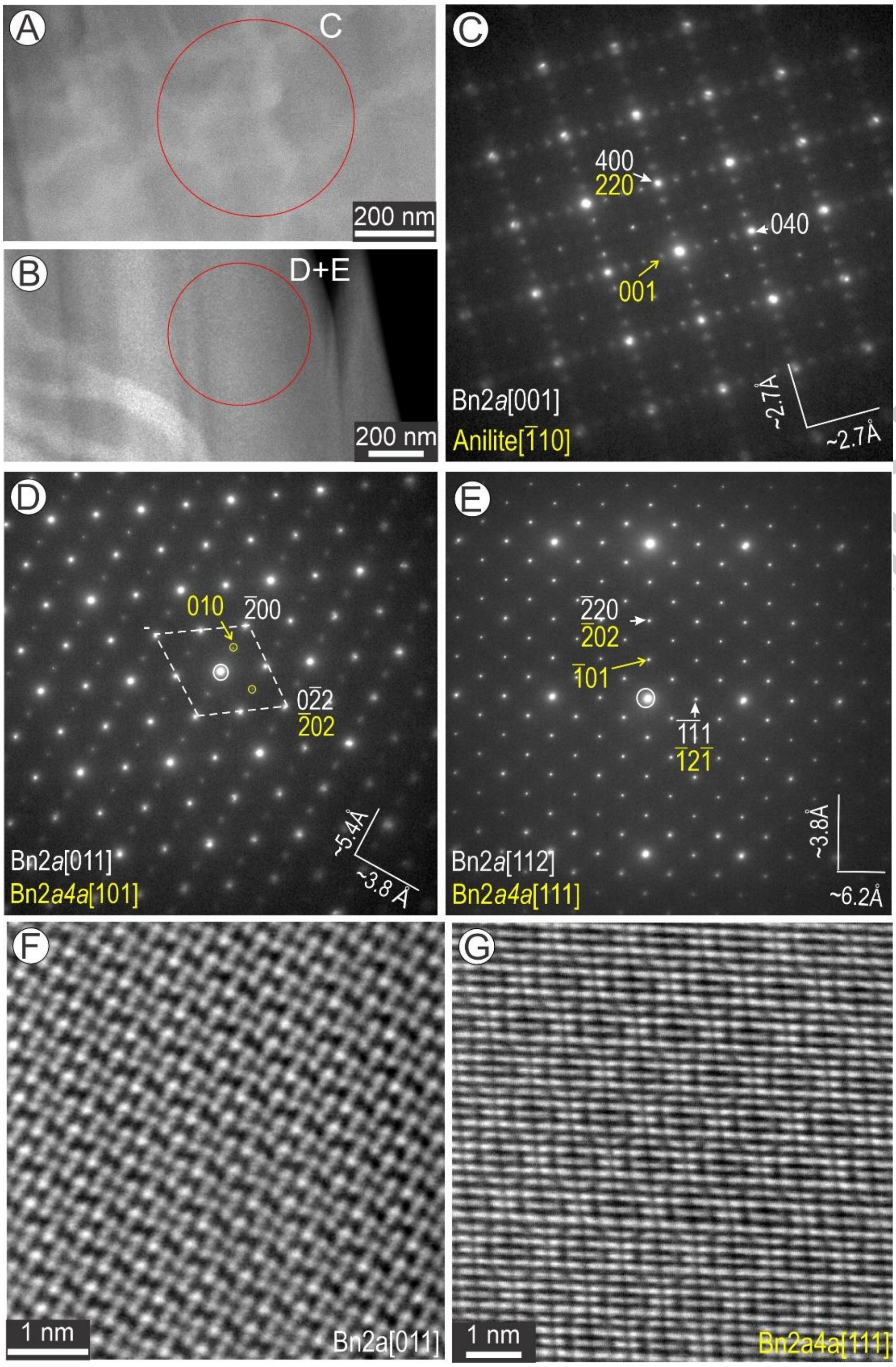

Figure 9. Two-phase association between bornite 2*a* (Bn2*a*) and Bn2*a*4*a* tilted on two zone axes as labelled. (A-C) Large image, crops and FFT patterns of [111] Bn2*a*4*a* (B) and [112] Bn2*a* (C) showing the subtle differences in the structural motifs typical of the two phases. (D-F) Large image, crops and FFT patterns of [101] Bn2*a*4*a* (B) and [110] Bn2*a* (C) showing the subtle differences in the structural motifs typical of the two phases. Dashed line shows the contact between the two phases.

Plane directions are indicated for each phase showing epitaxial relationships. (G) ED patterns and STEM simulations for the two phases on zone axes as labelled. The [110] Bn2*a* is shown in Figure 6E.

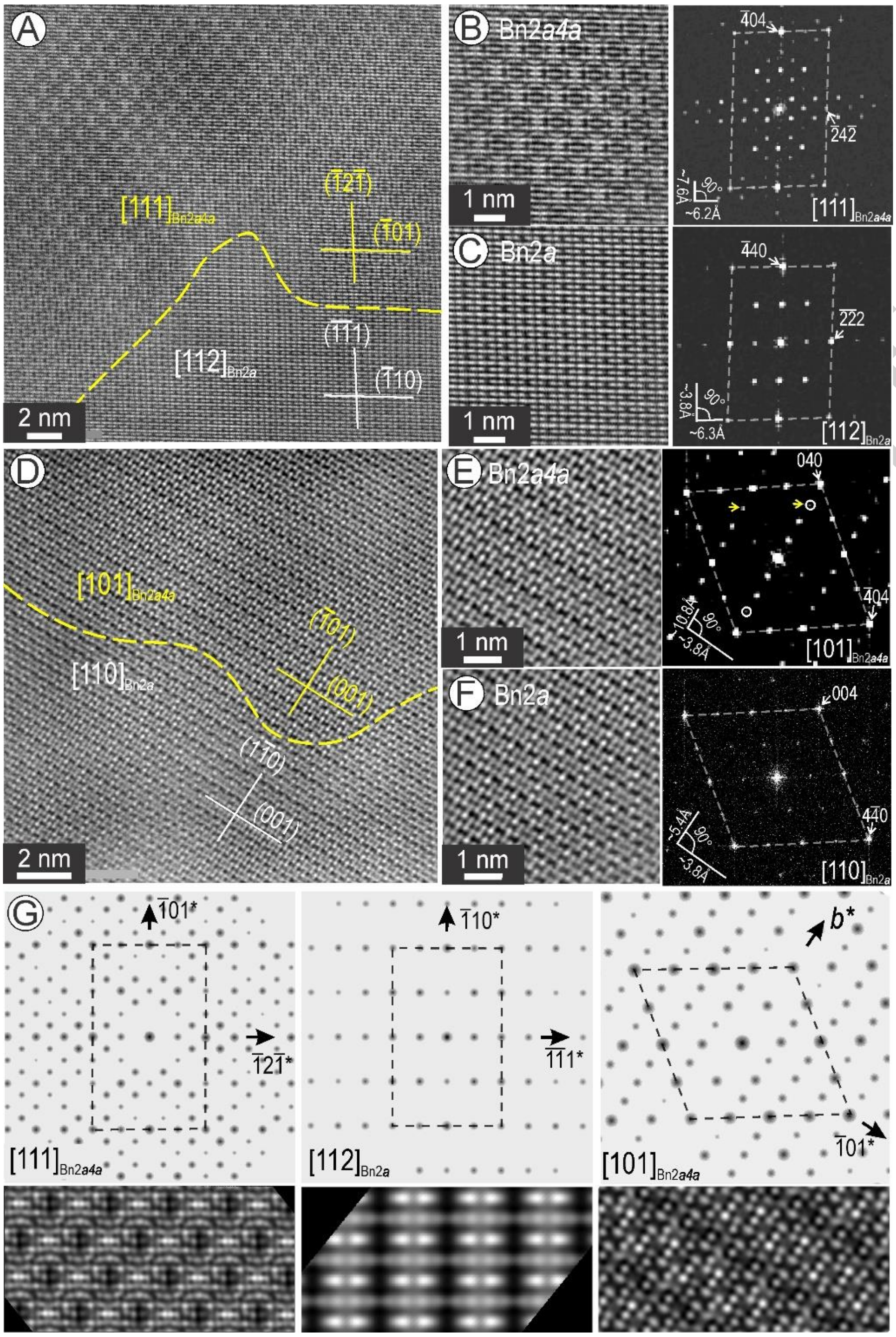

Figure 10. Two-phase association between digenite 1*a* (Dg1*a*) and bornite 2*a* (Bn2*a*) on three zone axes as labelled. (A, B) Images and corresponding FFT patterns (inset) for Bn2*a* and Dg1*a* on [100] in (A) and [110] in (B). The motifs corresponding to each phase are outlined on image crops beneath

each. (C) Defect (dashed line) between Bn2*a* and Dg1*a* on [110] orientation; FFT patterns as insets. (D) Image and FFT patterns as insets for Bn2*a* and Dg1*a* on [112] zone axis.

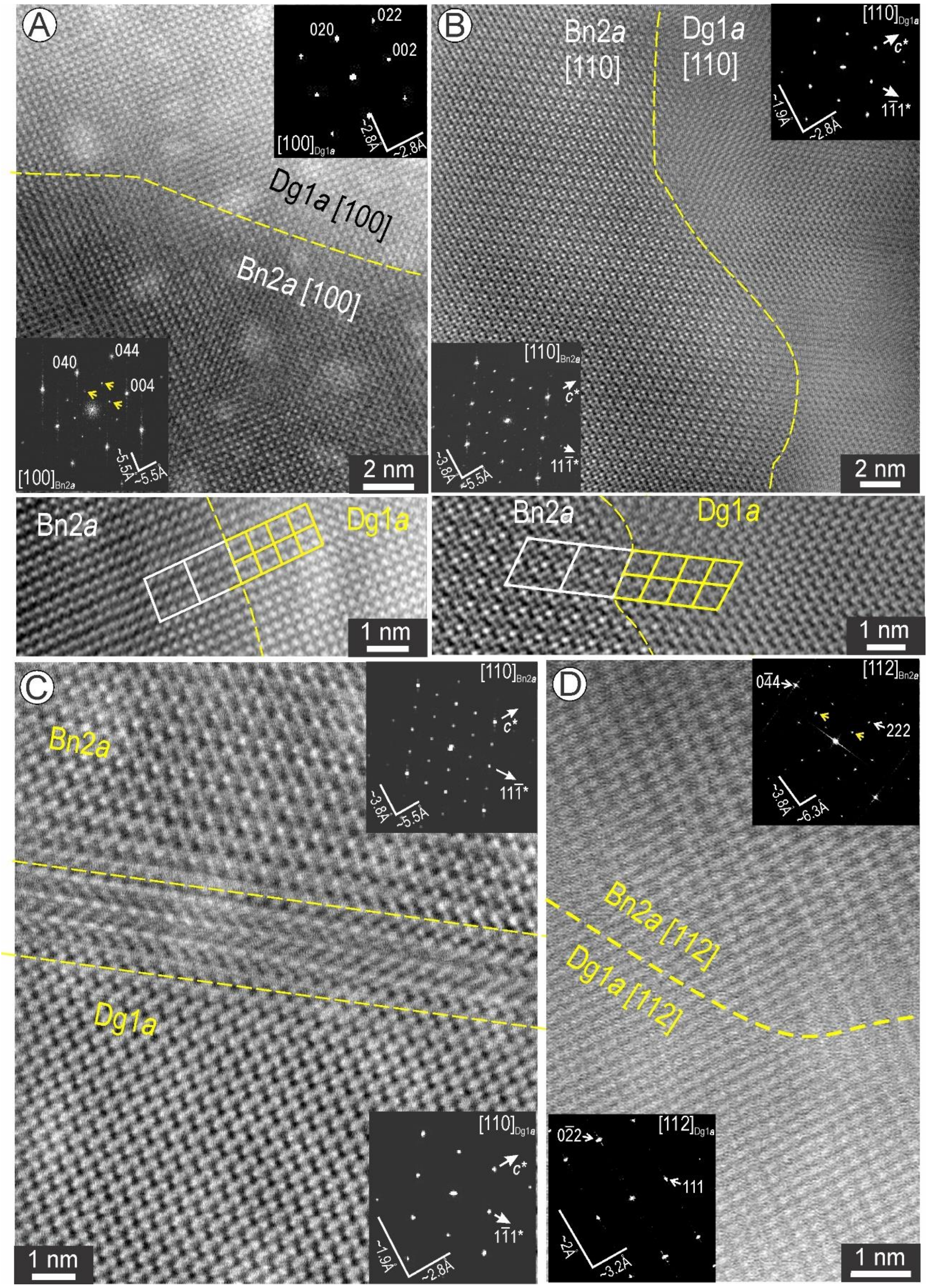

Figure 11. Two-phase association between bornite 2*a* (Bn2*a*) and digenite 3*a* (Dg3*a*) tilted on [110] zone axis. (A) Image and corresponding FFT pattern as inset showing the superposition of satellite reflection son <111>* directions. (B, C) FFT patterns obtained from each domains depicting the 3- and 2-fold satellite reflections corresponding to Dg3*a* and Bn2*a*. (D) Crop from (A) with outlines of the superstructures for each domain. (E) Spectra obtained from the two domains indicating the decrease in Fe content as labelled.

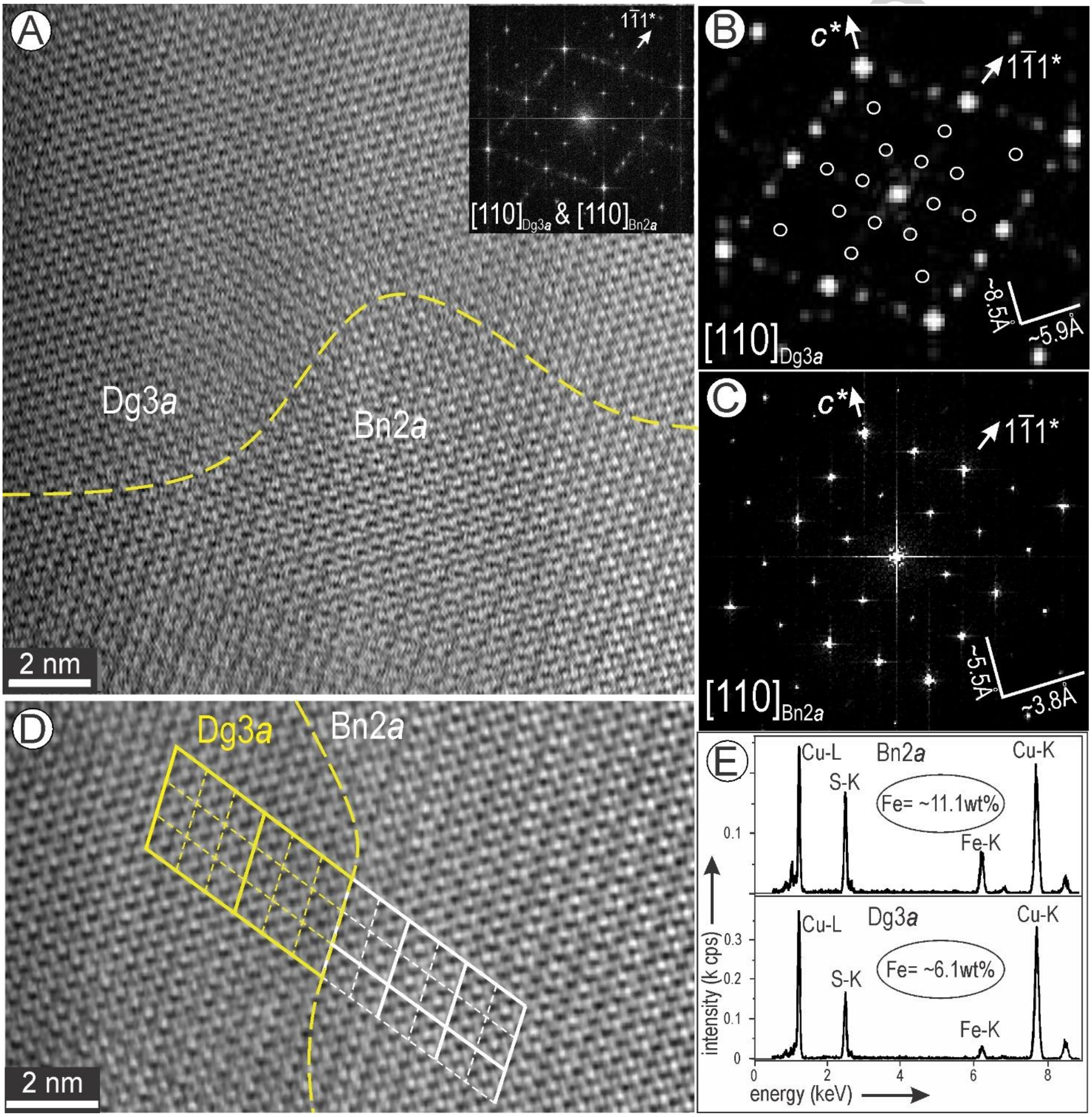

Figure 12. Intergrowths between [$\bar{1}$20] anilite (An) within [110] bornite 2*a* (Bn2*a*). (A, B) High-resolution images showing the coherence between planes (arrowed) of the two structures albeit with a stepwise defect in (B). (C) FFT pattern representing the image in (A) showing the overlap between the two structures. (D, E) FFT patterns obtained from each phase imaged in (B). (F, G) Simulation of anilite on [$\bar{1}$20] zone axis. (H) Crop of image in (B) showing the match with simulation in (G).

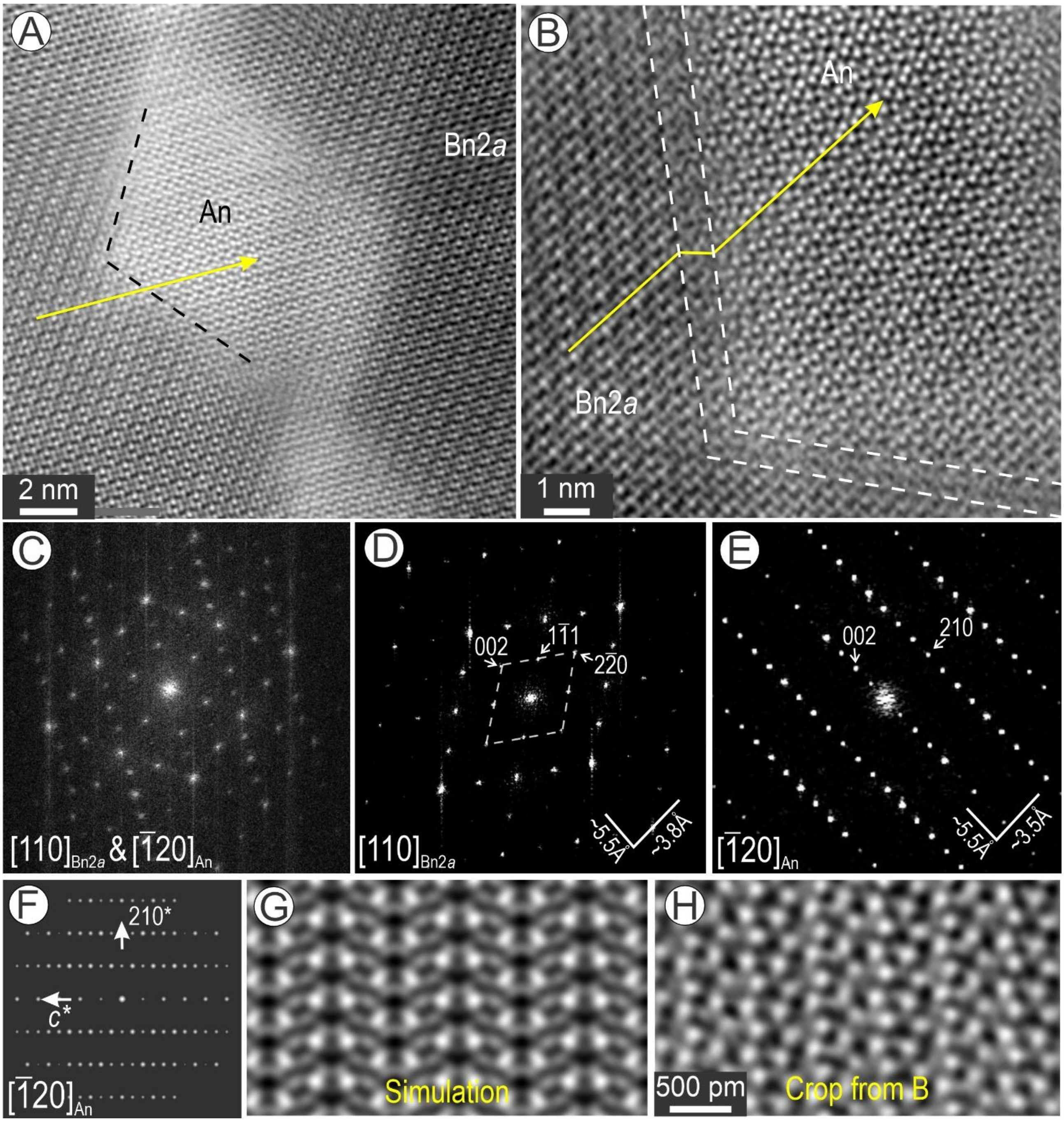

Figure 13. (A-C) Two-phase association between [$\bar{1}10$] anilite (An) and [100] bornite 2*a* (Bn2*a*) with corresponding FFT patterns in (B, C). (D-F) ED pattern, STEM simulation and image (crop from (A) showing An on [$\bar{1}10$] zone axis. (G) Image of [$\bar{1}10$] An and [001] chalcopyrite (Ccp). FFT pattern in the inset shows Ccp with satellite reflections (circled) indicative of a two-fold superstructure. (H) Spectrum of chalcopyrite obtained from spot in (G). Crop of image in (G) showing the 2-fold Ccp superstructure as brighter dots.

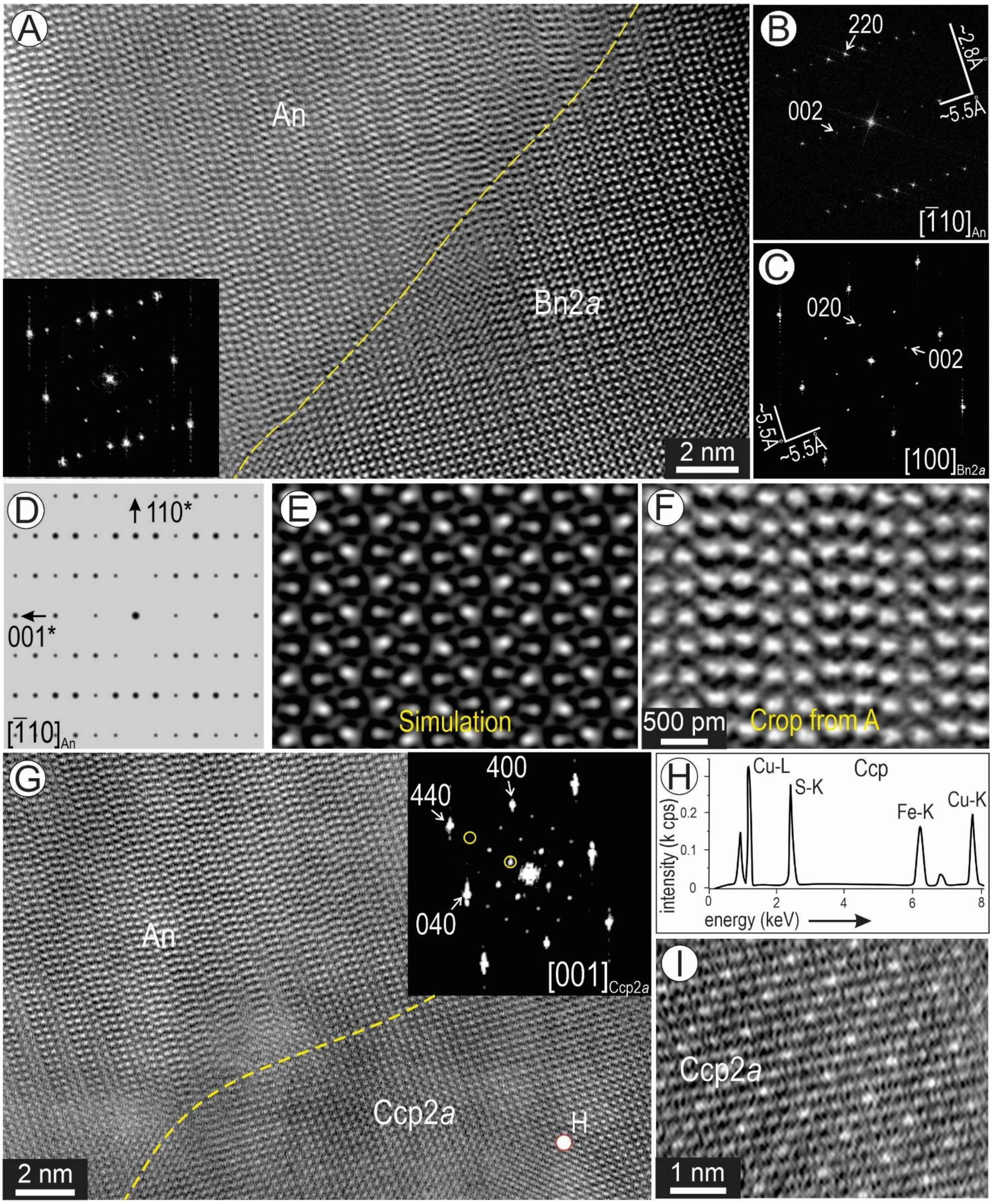

Figure 14. Bornite (Bn) from Fe-rich domains displaying rhythmically banded strips interpreted as Bn2*a*6*a* superstructure. (A-C) High-resolution images and FFT pattern in (B) showing the 2- and 6-fold satellite reflections (arrowed) along 111* bornite directions. Dark and bright intervals correspond to *c* lengths in 2*a* and 4*a* bornite as labelled. Inset in (C) is a crop showing closer detail of the bright

and dark strips. (D) Spectra of Fe-rich bornite obtained from maps as labelled. (E) Different orientation of the same Bn2*a*6*a* superstructure shown as a high-resolution image with bright and dark strips. (F) Corresponding FFT pattern displaying the same 2- and 6-fold satellite reflections (arrowed) along two directions in bornite. (G) Contact between [112] Bn2*a* and the inferred Bn*2*a6*a* with the same orientation as in (E). (H) FFT patterns showing additional satellite reflections (arrowed) along 111* due to the intergrowth with Bn*2*a6*a*.

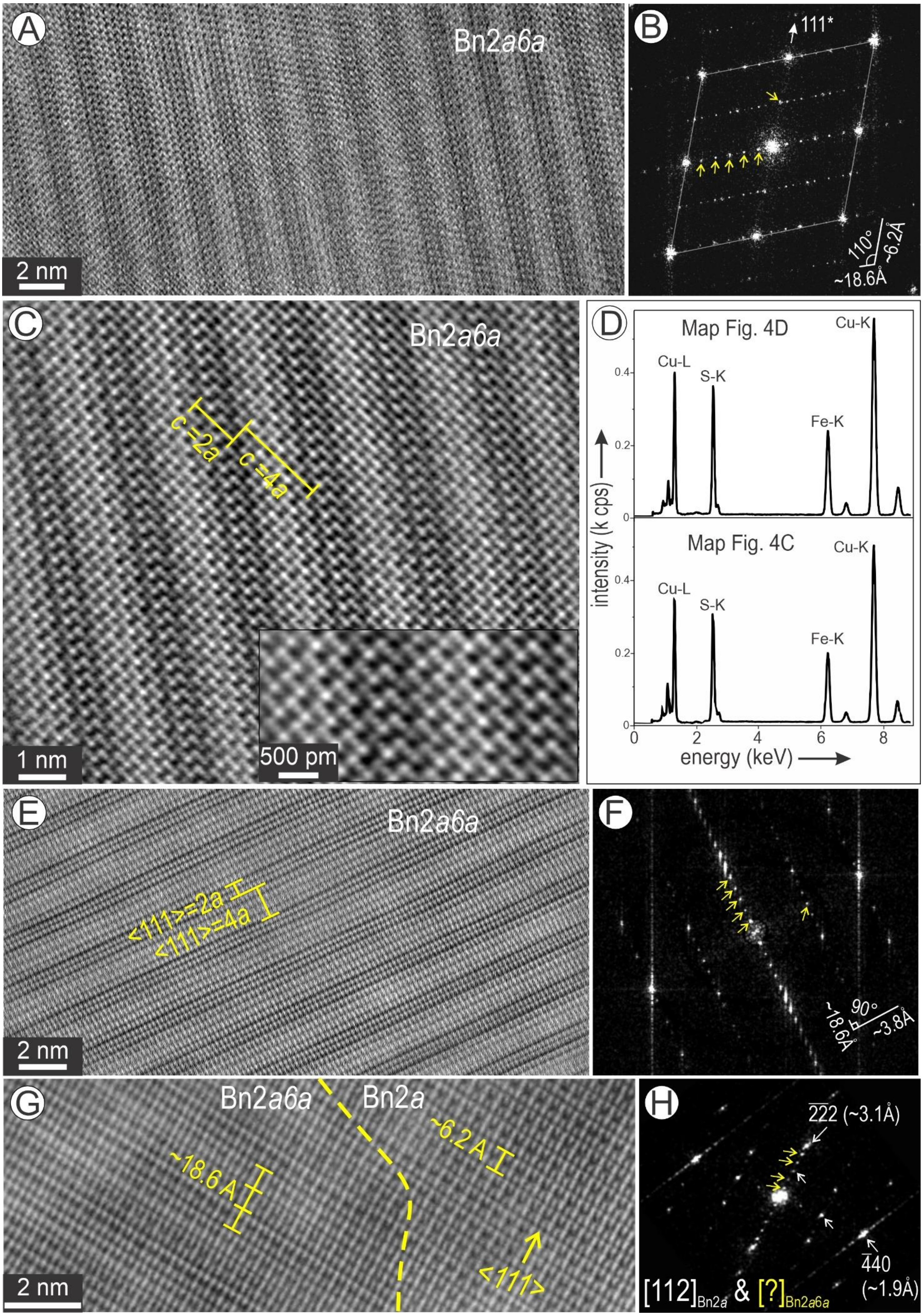
A
Bn2a6a
2 nm
B
111*
110°
~6.2Å
~18.6Å
C
Bn2a6a
c =2a
c =4a
1 nm
500 pm
D
Map Fig. 4D
Cu-L
S-K
Fe-K
Cu-K
Map Fig. 4C
intensity (k cps)
0.4
0.2
0
energy (keV)
0 2 4 6 8
E
Bn2a6a
<111>=2a
<111>=4a
2 nm
F
90°
~18.6Å
~3.8Å
G
Bn2a6a
Bn2a
~6.2 A
~18.6 A
<111>
2 nm
H
$\overline{2}\overline{2}2$ (~3.1Å)
$\overline{4}40$
(~1.9Å)
$[112]_{Bn2a}$ & $[?]_{Bn2a6a}$

Table 1. Details of STEM foils produced for nanoscale characterisation

No.	**Foil**	**Zone**	**Depth**	**Foil location**	**Major species**					**Min**	
			(-RLm)		Bn2*a*	Dg1*a*	An	Bn2*a*4*a*	Needle	Dg3*a*	B
1	RX6605-1	Bn-Cc	477.5	Coarse Bn-Cc symplectites	X	x	X		x	x	
2	RX6605-2	Bn-Cc	477.5	Coarse Bn-Cc symplectites	X	x	X	x	x		
3	CLC50a-1	Bn-Cc	554.9	Finest Bn-Cc symplectites	X	X	x				
4	CLC50a-2	Bn-Cc	554.9	Contact between Bn and lamellae of Cc	X	x	X	x	x		
5	RX6610-1	Bn-Cc	497.9	Purple bornite with lamellar networks	X	x	X	x	X		
6	RX6610-2	Bn-Ccp	497.9	Brown bornite with Ccp lamellae	X	x	X	x	X		
7	MV46	Bn-Ccp	359.4	Brown bornite without Ccp lamellae	X	x	X	x	x		

The relative occurrence of main species is indicated by: X (most abundant) and x (less abundant).
Abbreviations: An–anilite, Bn–bornite, Cc–chalcocite, Ccp–chalcopyrite, Dg–digenite.